Responses to the reviewers are uploaded separately. Since the font and font size is fixed during the upload progress in GMD, the major and minor reviewer comments are numbered, with our responses indented.

REFEREE 1 COMMENTS:

> We thank the reviewer for the thoughtful comments and suggestions and for their careful reading of our contribution.

Major comments:

(1) The study presented in this manuscript does not differentiate between deviations due to the simulation of the magnitude of the ambient wind speed and those due to inabilities of the wind farm parametrization (WFP). The WFP is not introduced in any detail and none of the found deviations is attributed to any feature of the WFP.

> Thank you for the suggestion that we discuss the WFP in more detail. However, we are not introducing the WFP to the literature (as it has already been introduced by Fitch et al. (2012), as cited in our manuscript. Nevertheless, we now provide a brief summary of the WFP equations in section 2.2 for the interested reader.
>
> The following is added to the manuscript, in lines 141 to 158:
>
> “The WFP scheme simulates wind farms and their meteorological influences to the atmosphere. We provide a brief summary here, and the details are discussed in Fitch et al. (2012). Wind turbines slow down ambient wind flow and convert a part of the kinetic energy of wind into electrical energy. The WFP represents this wind-turbine drag force as the kinetic energy harvested by the turbine from the atmosphere:

$$\boldsymbol{F}_{drag} = \frac{1}{2} C_T(|\boldsymbol{V}|)\rho|\boldsymbol{V}|A\boldsymbol{V},$$

where C_T is the turbine-specific thrust coefficient (discussed in detail in Fitch, 2015), $\boldsymbol{V}$ is the horizontal velocity vector, ρ is air density, $A = \frac{\pi}{4}D^2$ and is the cross-sectional rotor area, and D is the rotor diameter. This kinetic-energy extraction also causes changes in the atmosphere, namely the kinetic energy loss in the grid cell, which is described by the momentum tendency:

$$\frac{\partial|\boldsymbol{V}|_{ijk}}{\partial t} = \frac{N_t^{ij} C_T(|\boldsymbol{V}|_{ijk})|\boldsymbol{V}|_{ijk}^2 A_{ijk}}{2(z_{k+1}-z_k)},$$

where i, j, and k represents the zonal, meridional, and vertical grid indices, N_t^{ij} is the number of wind turbines per square meter, and z_k is the height at model level k. Of the kinetic energy extracted by the turbines, the WFP accounts for the electricity generation with:

$$\frac{\partial P_{ijk}}{\partial t} = \frac{N_t^{ij} C_P(|\boldsymbol{V}|_{ijk})|\boldsymbol{V}|_{ijk}^3 A_{ijk}}{2(z_{k+1}-z_k)},$$

where P_{ijk} is the power output in the grid cell in Watts, and C_P is the power coefficient. Assuming negligible mechanical and electrical losses, the rest of the kinetic energy harvested turns into TKE:

$$\frac{\partial TKE_{ijk}}{\partial t} = \frac{N_t^{ij} C_{TKE}(|\boldsymbol{V}|_{ijk})|\boldsymbol{V}|_{ijk}^3 A_{ijk}}{2(z_{k+1}-z_k)},$$

where TKE_{ijk} is the TKE in the grid cell, and C_{TKE} is the difference between C_T and C_P."

Further, we did consider approaches for distinguishing between "deviations due to the simulation of the magnitude of the ambient wind speed and those due to inabilities of the WFP", but because there was no systematic bias (or even a stability-dependent bias) in the simulation of the ambient wind speed, such a differentiation is not possible. And in fact, performing and comparing idealized WRF simulations will address the implications of representing ambient wind speed accurately, while herein, we simulate a real case study since we aim to verify modelled power production with the observed. The focus here was on whether or not, as it stands, the WRF-WFP offers value beyond WRF itself, which had not yet been demonstrated in past research. Attributing the deviations to the features of the WFP would require modifying those features, which would be the subsequent step in this research.

(2) Mesoscale models such as WRF are known to underrepresent the nocturnal low-level jet phenomenon. This has been analysed and explained by Sandu et al. (2013). Deviations in simulated power due to deviations in simulating the ramp effects at the onset of low-level jets (LLJ) have to be attributed to WRF itself and not to WFP. With regard to this known feature it seems a bit unlucky to choose a LLJ episode for this WFP evaluation.

Thank you for the suggestion to include Sandu et al. (2013) in our literature review. Their analysis of the model performance of the 2011 version of the ECMWF model has some similarities with the current WRF framework. They note that “The ECMWF model operational in 2011 reasonably represents this diurnal cycle of wind but underestimates its amplitude both at the surface and at 200 m.” This type of behaviour is focused on how the ECMWF model predicts annual averages at the Cabauw tower, and is not borne out in WRF simulations in the Midwestern United States as well as Hamburg, Germany, as studied by Jahn et al. (2017), where they show some under-predictions as well as over-predictions, due to reductions in the stable layer surface mixing in the MYNN scheme used herein.

Rather than being “unlucky” in our selection of cases, we specifically selected this case study because of the importance of LLJs to wind energy. Vanderwende et al. (2015) have also simulated the LLJ phenomenon for this case study. They found the WRF model overall is skilful in simulating these LLJ events, as also demonstrated by our simulations. Moreover, LLJ events provide substantial wind resources, and verifying the WRF WFP in this period with ample power production is appropriate.

Although Sandu et al. (2013) tested the impact of turbulence diffusion and turbulence closure using the ECMWF model, we do specifically acknowledge the potential influence of turbulence parameterization in the revised version of the paper. Lines 345 to 347 now read "Reducing turbulence diffusion in the WRF model could potentially yield more accurate simulated winds in stable conditions, including LLJs (Sandu et al., 2013); active research in modifying mixing lengths (Jahn et al., 2017) is suggesting promising results."

(3) The lower right frame of Fig. 8 shows the dependence of the bias of the simulated power output from atmospheric stability. The authors interpret this figure as showing no significant dependence. My impression is, if the very few data points beyond the stability of 0.6 are skipped, that there is a significant influence of atmospheric stability (leading to a negative bias for more stable situations).

This is an interesting suggestion. If we remove the strong stability points ($z L^{-1}$ larger than 0.6), a weak negative correlation of -0.61 emerges. The dependence of negative power bias and stable atmosphere does increase when only data of accurately simulated WS and WD are considered (Fig 8d and the new Fig. 9d).

Therefore, we now state in lines 283 to 286 that "Moreover, when considering only cases of accurate wind predictions, the correlation between power bias and stability increases from -0.06 (Fig. 8d) to -0.42 (Fig. 9d). If the few strongest stability points ($z L^{-1}$ larger than 0.55) are removed from the analysis, a weak negative correlation with stability emerges as the Pearson correlation coefficient becomes -0.61."

(4) The discussion section (Section 4) makes reference to several results which have not been shown in the preceding results section (Section 3). Therefore, the reader cannot prove these conclusions.

Thank you for your comment. An introduction to the 2-sample t-test and the results from Table 6, 7 and 8 are now discussed in the results section. Lines 237 to 246 now read "Moreover, to statistically differentiate the power productions from various model runs, we apply the 2-sample Student's t-test. The null hypothesis of a 2-sample t-test is that the two population means are the same, assuming the underlying distributions are Gaussian (Wilks, 2011). Hence, if the resultant p-value is equal to or below 0.05, the two distributions are statically significantly different at the 95% confidence level. For example, the difference between the 4-day power-production averages from the ERA12 and from the ERA12WF is -46.8 MW. The respective p-value is 0, thus the difference of the means is statistically significant (Table 6). In other words, the ERA12 and the ERA12WF yield different power production distributions. Similarly, the GFS12 and the GFS12WF lead to statistically different power outputs as the p-value from t-test is 0 as well (Table 7). We also use the 2-sample t-test to contrast the actual and the modelled power distributions. For instance, all the p-values between the no-WFP runs and the observation are 0, implying those simulations yield power distributions significantly different from the reality (Table 8)."

(5) The main conclusion that simulations with WFP are better than those without it is quite trivial.

In addition to our suggestion to use the WFP, we quantify the power-error reduction with the use of the WFP, and we verify the WFP power by demonstrating the model power bias under different circumstances including ambient wind speed and turbulence. We address questions of performance such as the number of turbines per cell, etc. to help diagnose potential issues with the WFP. We construct the verifications based on the usefulness of the WFP, which is one of the key elements of this study.

(6) The study does not present any points which would allow for an enhancement of the simulation tool (either WRF or WFP or both). (Please refer to comment (1) above as well)

We suggest that improving the wind speed prediction in the WRF model is the key to improve the skills of the WFP. Please see lines 347 to 349, "More importantly, improving the skills of the WRF model in simulating WS can improve the WFP power performance (Fig. 10). Future versions of the WRF model as well as the WFP should aim to better account for instantaneous horizontal WS variations and the subsequent sub-gird wake interactions."

(7) sigma_u and sigma_w cannot be derived from a single monostatic remote sensing device (be it a sodar or a lidar) operating in Doppler beam swinging mode. Thus, the variables TKE and TI (equations (1) and (2)) are very unsure and cannot be used for a reliable evaluation study. This problem can be easily seen from the massive scatter of the TKE values in the third frame of Fig. 7.

The TKE and TI in equations (1) and (2) are calculated using 2-minute averaged variances of the 3-dimensional wind components measured by the lidar, as stated in the manuscript (lines 254 to 256) and as discussed in previous work by our group and others (Kumer et al., 2016; Rhodes and Lundquist, 2013). The trends of the modelled and observed TKE's shown in Fig. 7c match well, although the methodologies behind the two TKE's are spatially, temporarily and mathematically different.

To emphasize the differences between the TKE produced by the WRF model and the TKE derived from the lidar, lines 254 to 257 now read "Note that in Fig. 7c, the lidar derives TKE using 2-min variances, which is intrinsically different from the modelled TKE, as discussed in Rhodes and Lundquist (2013) and Kumer et al. (2016). Hence, readers should focus on the general trends of the TKE time series, rather than their absolute values."

Minor comments:

(8) The analytic wind farm model in Emeis (2010) is not based on an exaggerated surface roughness. This model uses the farm-averaged thrust coefficient of the wind turbines to extract momentum at hub height. In doing so the model considers a modified surface stress due to the wind farm as well. Please update the paragraph (lines 31 to 37).

Thank you for the clarification. After revisiting Emeis (2010), we agree that the effective roughness length at hub height depends on the effective drag coefficient, which is a sum of both the areal average of momentum extraction coefficient of turbines (or thrust coefficient, as mentioned in your comment) and the surface drag coefficient.

Lines 34 to 37 now read "Similarly, the analytical wind park model of Emeis and Frandsen (1993) considers both the downward momentum flux and the momentum loss due to surface roughness. The revised model by Emeis (2010) accounts for the spatially-averaged momentum-extraction coefficient by turbines, and the parameters become atmospheric-stability dependent."

(9) The explaining text accompanying the figures in the results section (Section 3) is sometimes quite short.

The results section now includes the following text:

Lines 191 to 195 now read "The 200S records the vertical shear caused by LLJs above 100 m (Fig. 3a), and the WC measures the near-surface winds with high temporal resolution (Fig. 3b). In both the observations and the simulations of WS (Fig. 3c), the night-time WS profile is stratified and the daytime atmosphere is well-mixed. The WD simulations also match well with the measurements, where in the evening the winds veer, or turn clockwise with height (Fig. 4), while the daytime flow shows relatively constant wind direction with height."

Lines 214 to 216 now read "We present the total 10-min observed and simulated power of the whole wind farm at the bottom of each panel in Fig. 5, where the total power production of the WFP run matches the observed."

Based on the new Fig. 9, lines 279 to 287 now read "To isolate the WFP errors in power predictions from the WRF model errors in ambient wind simulations, we analyse a subset of data where the winds are simulated accurately. When the absolute error in wind speed is smaller than 1 m s^{-1} and the absolute error in wind direction is smaller than 5°, the relationships between power bias and WS, WD and TI (Fig. 9a to c) remain similar to the general trends shown in Fig. 8a to c. The WS-power-bias and TI-power-bias correlations become stronger in this subset (Fig 9a and c), compare with all the data in the 4-day period (Fig 8a and c). Moreover, when considering only cases of accurate wind predictions, the correlation between power bias and stability increases from -0.06 (Fig. 8d) to -0.42 (Fig. 9d). If the few strongest stability points (z L^{-1} larger than 0.55) are removed from the analysis, a weak negative correlation with stability emerges as the Pearson correlation coefficient becomes -0.61. Additionally, generally south to south-westerly flows yield stronger negative power biases."

In lines 303 to 308, "Furthermore, the WFP performance remains consistent between upwind and downwind turbines, based on their positions against the ambient winds (Fig. 12). Given the square shape of grid cells, we determine the sequential rows of turbines during strictly southerly flows, with WD between 175° and 185° (Fig. 12a). The bulk of the normalized power biases fall within 0 to 0.4 MW, regardless of the upwind-downwind positions of turbines. Additionally, the power bias is independent of the mean distance between the actual turbine locations and the centre points of their respective grid cells (not shown)."

(10) The chosen colour scale of several figures (especially Figs. 3 and 5) should be improved. It is extremely difficult to see the small differences which are said to be important.

We have adjusted the dark end of the colour table for Figs. 3 and 5 to emphasize the range of values. Please see the revised figures below.

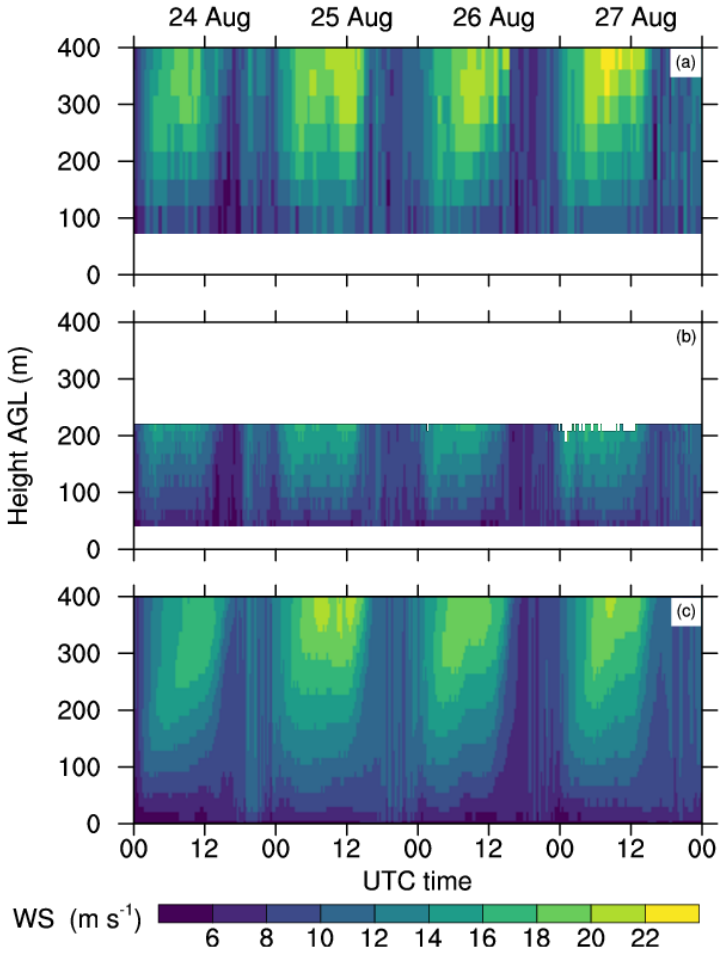

24 Aug
25 Aug
26 Aug
27 Aug
(a)
(b)
(c)
Height AGL (m)
400
300
200
100
0
00
12
UTC time
WS (m s-1)
6
8
10
12
14
16
18
20
22

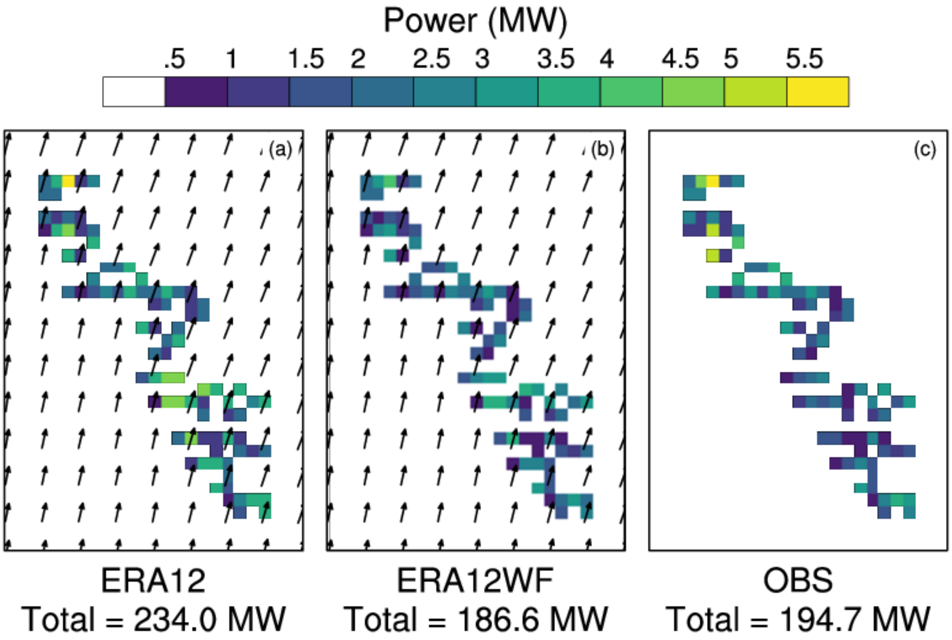
Power (MW)
.5
1
1.5
2
2.5
3
3.5
4
4.5
5
5.5
(a)
(b)
(c)
ERA12
Total = 234.0 MW
ERA12WF
Total = 186.6 MW
OBS
Total = 194.7 MW

220

REFEREE 2 COMMENTS:

We thank the reviewer for their careful reading of our manuscript and their comments and suggestions.

Major comments:

(1) At least 4 uncertainties in simulating the power production with mesoscale models can be thought of, due to (I) mismatches in wind speed and wind direction (II) errors in simulating the wind speed reduction between grid-cells (III) errors in grid-cell internal wind speed reduction (IV) errors in power production, since turbine positions remain unresolved.

A big challenge in estimating the power production correctly is that the grid-cell averaged wind speed from the mesoscale model is not necessarily equivalent to the local up-stream wind speed of a turbine. Especially, in the presented wind farm layout, where turbines are systematically aligned in the West-East direction, mismatches between simulated and measured power production are expected. For southerly/northerly (and also south-westerly) winds, turbines in the southern/northern most rows all experience free-stream wind conditions and produce accordingly. On the other hand, the model wind speed in each turbine containing grid-cell is reduced due to the drag of all turbines in that grid-cell, leading to a systematically underestimated modelled power production. For easterly/westerly wind directions, the opposite happens and the interaction between turbines is underestimated, since in the model the turbine interaction is only area averaged.

Unfortunately, for the 4 day campaign not all wind directions are observed. However, there are examples that clearly show the challenges. On day 4 with south-westerly winds a large fraction of the turbines experience free-stream conditions, leading to large productions, whereas the modelled power production was systematically too low. For events with southerly winds the situation is more complex, since only the front turbine rows experience free-stream conditions and all other turbines are affected by wind farm internal wakes.

Therefore, a deeper analysis on when and why the model is able/unable to estimate the power production is recommended. First, only events in which the wind speed and wind direction were modelled correctly should be included for the verification. Perhaps, in the scatter plots filled and empty circles could be used to distinguish events that were inside or outside the filter criteria.

One example: since Fig.9 shows that also for events with around 0 m/s bias the power production bias ranges from around -70 to 90MW, it could be interesting to plot similar to Fig 8a the bias in power production against the modelled wind, but only for events where the wind speed bias was smaller than e.g. 2m/s and the wind direction bias smaller than e.g. 30°. In this plot the colours could be used to indicate the wind direction instead of the days. This would allow see the ability of simulating the power production for different wind directions.

For the above mentioned reasons, I would not agree with the conclusions made from the wind direction sensitivity analysis on p. 8 l. 228, given that the behaviour for the South-Westerly directions is very distinctive from other directions.

> Thank you for the thoughtful suggestion. According to your suggestion, we produce the following plot as the new Figure 9. This figure replicates Fig. 8, while only the data with the modelled-observed absolute error in wind speed smaller than 1 m s^{-1} and the absolute error in wind direction smaller than 5°. In other words, the WRF model reproduces accurate ambient winds in these data points. Different colours represent different lidar-measured wind directions and the n’s are respective sample sizes.

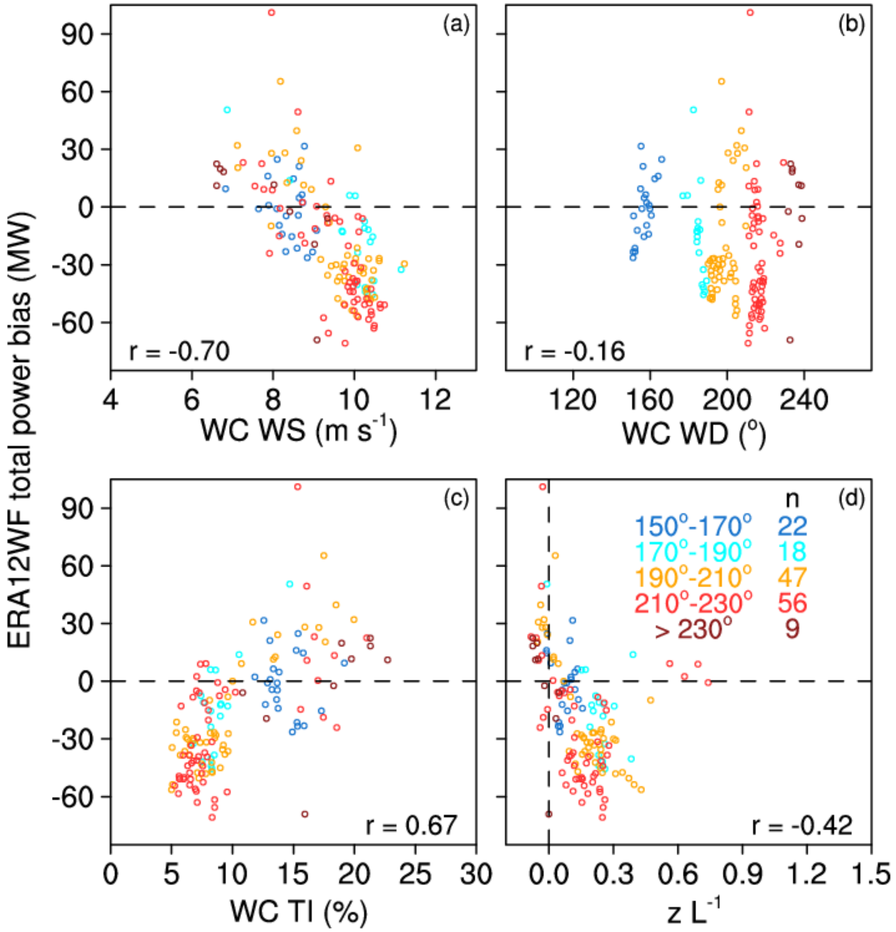

In Fig 8d, although the correlation between power bias and stability is only -0.06 if we include all the data points, when we only consider data points when the WRF model simulates accurate wind speed and wind direction, the correlation increases to -0.42.

In the new Fig. 9, the general trend of the negative relationship between power bias and measured wind speed shown in Fig. 8a remains prominent. When wind speed is below 9 m s^{-1}, power bias is mostly above -30 MW, regardless of wind direction.

From the new Fig. 10 (the original Fig. 9), power bias overall is positively correlated with wind speed bias, such that overestimating wind speed leads to power overestimation. The new Fig. 9

shows that even without large errors in simulating wind speed and wind direction, strong winds (in this case, wind speed at around and beyond 10 m s^{-1}) actually lead to under-prediction of power. The power underestimation is associated with southerly to south-westerly winds, and the respective wind speeds are also relatively large. Hence we cannot confidently conclude the interactions between wind direction and wind-farm layout and their resultant influence on power production and wake effects as suggested by the reviewer.

One possible factor contributing to the consistent underestimation of power production during south-westerly flow is the wake interactions within a grid cell. However, we have already shown that inter-cell wake effects are not the critical factor to power error (the new Fig. 12b). The inability of the WFP to simulate intra-cell wake effects can explain the large negative biases when many of the turbines experience unobstructed south-westerly flow.

Based on the new figure, the following are added to the text. In lines 279 to 287 (the results section),

“To isolate the WFP errors in power predictions from the WRF model errors in ambient wind simulations, we analyse a subset of data where the winds are simulated accurately. When the absolute error in wind speed is smaller than 1 m s^{-1} and the absolute error in wind direction is smaller than 5°, the relationships between power bias and WS, WD and TI (Fig. 9a to c) remain similar to the general trends shown in Fig. 8a to c. The WS-power-bias and TI-power-bias correlations become stronger in this subset (Fig 9a and c), compare with all the data in the 4-day period (Fig 8a and c). Moreover, when considering only cases of accurate wind predictions, the correlation between power bias and stability increases from -0.06 (Fig. 8d) to -0.42 (Fig. 9d). If the few strongest stability points ($z L^{-1}$ larger than 0.55) are removed from the analysis, a weak negative correlation with stability emerges as the Pearson correlation coefficient becomes -0.61. Additionally, generally south to south-westerly flows yield stronger negative power biases.”

In lines 350 to 358 (the discussion section),

“Besides necessary improvements in simulating ambient WS, the WFP scheme itself also requires refinements. When background winds are accurately predicted, the power-bias dependence on WS and TI remain strong (Fig. 9a and c). Although the relationship between the WFP performance and stability is generally indistinct, the correlation becomes weakly negative without the strongly stable data. Even when the simulated winds are close to observations, the WFP underestimates power during high WS, south to south-westerly flow, low TI and stable conditions. Certainly the interactions between WD and wind-farm layout affect the power-bias relationships, while further sensitivity tests can further upgrade the WFP performance, particularly in intra-cell WS reduction. We demonstrate that inter-cell wake effects are not the critical factor to power error (Fig. 12b), hence the inability of the WFP to simulate intra-cell wake effects can explain the biases when many of the turbines experience accurately-simulated ambient flow.”

(2) I agree that the model’s performance is most likely not sensitive to the number of turbines per grid-cell, but is important to find out how sensitive it is to the turbine positions in the grid-cell.

Following the suggestion, we have explored different ways of considering the turbine positions in the grid-cell, and we found no sensitivity. Below we first show the mean power bias in each turbine-containing grid cell of the ERA12WF simulation as a function of the mean distance between the actual turbine locations and the centre point of their respective grid cells, within a grid cell.

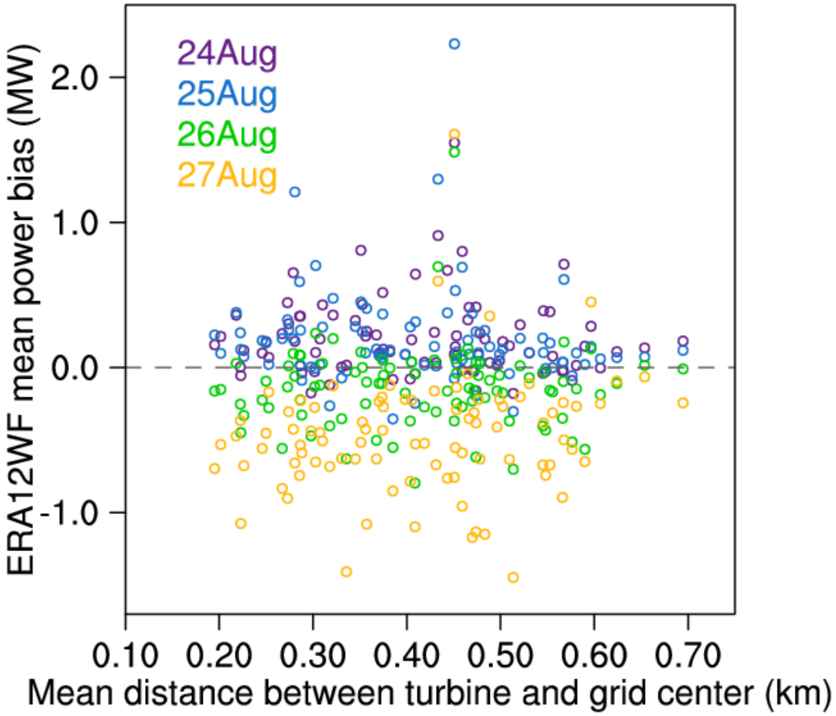

In this second plot below, we look at only the north-south distance within the cell, between the actual turbine location and the grid cell centre. The x-axis below is the sum of distances between turbine latitude and grid centre latitude, based on the longitude of the grid cell centre point. Positive values indicate the wind turbine location is south of the grid centre, or grid centre latitude is larger than the turbine latitude. Negative values indicate the wind turbine location is north of the grid centre. The 4-day correlation is 0.23.

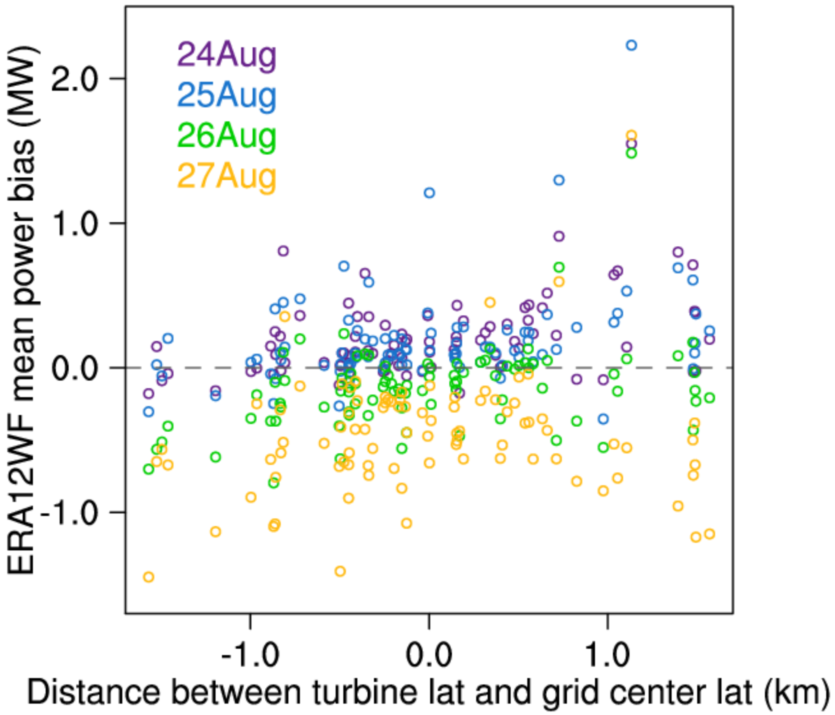

When the turbine locations are farther from the centre of a grid cell, the power bias stays relatively consistent around zero. The lack of a distinct relationship between power bias and observed-modelled distance demonstrates that the turbine position in grid cell does not have a significant role in power error. This is reasonable since the mesoscale WRF model indicates turbines and their effects across the whole grid cell, as long as they are within that grid cell.

These results are added to the text, in lines 306 to 308, “Additionally, the power bias is independent of the mean distance between the actual turbine locations and the centre points of their respective grid cells (not shown).”

Minor comments:

(3) p.2 l.57-59, WEP should be replaced with EWP.

All the “WEP” are now corrected to “EWP”. Thank you.

(4) p.4 l.114-123, in this paragraph measurements from the surface flux station are introduced. However, only the power bias against stability (Fig.8d) has been shown without showing the model’s ability to simulate stability. For this figure to become more meaningful the model surface layer stability could be compared to that measured.

Since stability parameters like Obukhov length are not the standard output variables of the WRF model, we use the sensible heat flux to represent stability in the revised Fig. 7d.

Lines 252 to 254 now read, “Although the magnitudes of the surface sensible heat flux of the surface flux station and the simulations differ, their signs change at similar times, particularly in the last three days (Fig. 77d). Hence the WRF model is capable to represent diurnal atmospheric stability changes.”

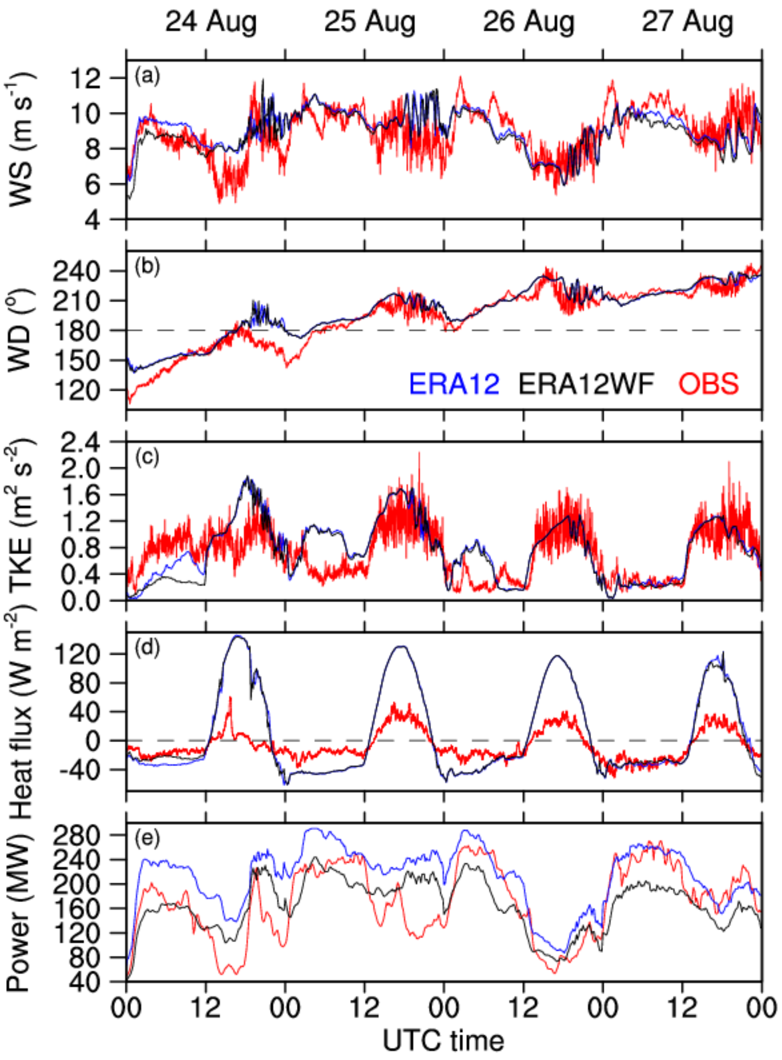

(5) In the comparison of the TKE, it should be mentioned why the TKE derived from the Lidar measurements are expected to match the completely parametrised model TKE with a 1D production.

Similar to our answer to comment (7) of Referee #1, only the general trends of lidar TKE and model TKE should match, rather than their values. Lines 254 to 257 now read "Note that in Fig. 7c, the lidar derives TKE using 2-min variances, which is intrinsically different from the modelled TKE, as discussed in Kumer et al. (2016) and Rhodes and Lundquist (2013). Hence,

> readers should focus on the general trends of the TKE time series, rather than their absolute values."

(6) Fig. 7c, it is curious that the TKE of ERA12 is larger than that of ERA12WF as well in the night as during the day and that it seems never to be smaller. What would be your explanation for this?

> Most of the TKE deviations between the two simulations take place before 12 UTC on 24 August, where the ERA12 simulates higher wind speeds than the ERA12WF. The reduced wind speeds in the ERA12WF simulation can explain lowered TKE in the evening, as the vertical momentum transfer is obstructed.

(7) Regarding section 2.2, here the model set-up (namelists) should probably be made available to GMD.

> An example namelist is now uploaded to http://doi.org/10.5281/zenodo.847780 and the link provided in the revised version of the manuscript.

(8) p.5 l.134, the inner domain with a 1 kilometre grid-spacing extends over the whole state of Iowa. This seems a computational expensive solution. What was the motivation for this configuration. Did you perform a sensitivity to the domain size?

> We include the whole state of Iowa in the smallest domain in order to ensure the wind farm is near the centre of the domain, and not to be close to the domain edges. Since the wind direction changes over the four-day period, locating the wind site near the domain centre is an appropriate choice, even the domain can be slightly smaller. We did not perform any sensitivity study with respect to the size of the domain. Moreover, simulating the whole state of Iowa also provides model data for future meteorological comparisons in other sites in western Iowa with wind farm

data that our group is in the process of acquiring (as in Walton et al., 2014), so the model simulation output will be used for other purposes as well.

(9) In Fig. 3, it would be helpful to indicate the periods in which the 200S lidar and the WC lidar are in the wake of turbines.

The wind direction changes from southeast to southwest during the 4-day period. The WC lidar measures ambient flow. The nearest upwind turbine, southeast of the WC lidar, is located over 32 D (2.7 km) away. Hence the WC observations are only potentially affected by wakes when the winds are south-easterly, which is during the first 30 hours of the case study. And at that distance, it would be remarkable for a wake to affect the WC.

The 200S lidar is 440 m north of a turbine row, so its measurements in the lowest 120 m of the atmosphere may have been waked on occasion. However, the 200S measurements used herein (Figs. 3 and 4) are primarily above the top of the turbine rotor disk (120 m) and would not be affected by wakes. We have now included a reference to a manuscript in which the 200S horizontal scans are used to understand turbine wake behaviour in this wind farm (Bodini et al., 2017).

We think adding the above as graphic indications would overcrowd the contour plots (Fig. 3 and Fig. 4), so we include these notes in the text. Lines 113 to 117 now read “Since the dominant wind directions during the campaign are south-easterly to south-westerly (Vanderwende et al., 2015), some of the 200S measurements below the rotor top (about 120 m AGL) could be influenced by turbine wakes during conditions, in which wakes persist longer than 5 D downwind from the turbine (Bodini et al., 2017). On the other hand, WC measurements are largely unaffected by turbine wakes except when WD is east of 150°. The closest upwind turbine during this simulation period was located over 2.7 km (33 D) to the southeast.” Moreover, lines 196 to 198 now read “The 200S measurements above the rotor layer (120 m) are unaffected by turbine wakes (Fig. 3a and Fig. 4a); the LLJs observed above the rotor layer resemble those from the ERA12, supporting the skills of the simulations.”

References

Bodini, N., Zardi, D. and Lundquist, J. K.: Three-Dimensional Structure of Wind Turbine Wakes as Measured by Scanning Lidar, Atmos. Meas. Tech. Discuss., 1–21, doi:10.5194/amt-2017-86, 2017.

Emeis, S.: A simple analytical wind park model considering atmospheric stability, Wind Energy, 13(5), 459–469, doi:10.1002/we.367, 2010.

Emeis, S. and Frandsen, S.: Reduction of horizontal wind speed in a boundary layer with obstacles, Boundary-Layer Meteorol., 64(3), 297–305, doi:10.1007/BF00708968, 1993.

Fitch, A. C.: Notes on using the mesoscale wind farm parameterization of Fitch et al. (2012) in WRF, Wind Energy, 19, 1757–1758, doi:10.1002/we.1945, 2015.

Fitch, A. C., Olson, J. B., Lundquist, J. K., Dudhia, J., Gupta, A. K., Michalakes, J. and Barstad, I.: Local and Mesoscale Impacts of Wind Farms as Parameterized in a Mesoscale NWP Model, Mon. Weather Rev., 140(9), 3017–3038, doi:10.1175/MWR-D-11-00352.1, 2012.

Jahn, D. E., Takle, E. S. and Gallus, W. A.: Improving Wind-Ramp Forecasts in the Stable Boundary Layer, Boundary-Layer Meteorol., 163, 423–446, doi:10.1007/s10546-017-0237-2, 2017.

Kumer, V.-M., Reuder, J., Dorninger, M., Zauner, R. and Grubišić, V.: Turbulent kinetic energy estimates from profiling wind LiDAR measurements and their potential for wind energy applications, Renew. Energy, 99, 898–910, doi:10.1016/j.renene.2016.07.014, 2016.

Rhodes, M. E. and Lundquist, J. K.: The Effect of Wind-Turbine Wakes on Summertime US Midwest Atmospheric Wind Profiles as Observed with Ground-Based Doppler Lidar, Boundary-Layer Meteorol., 149(1), 85–103, doi:10.1007/s10546-013-9834-x, 2013.

Sandu, I., Beljaars, A., Bechtold, P., Mauritsen, T. and Balsamo, G.: Why is it so difficult to represent stably stratified conditions in numerical weather prediction (NWP) models?, J. Adv. Model. Earth Syst., 5(2), 117–133, doi:10.1002/jame.20013, 2013.

Vanderwende, B. J., Lundquist, J. K., Rhodes, M. E., Takle, E. S. and Irvin, S. L.: Observing and Simulating the Summertime Low-Level Jet in Central Iowa, Mon. Weather Rev., 143(6), 2319–2336, doi:10.1175/MWR-D-14-00325.1, 2015.

Walton, R. A., Takle, E. S. and Gallus, W. A.: Characteristics of 50–200-m Winds and Temperatures Derived from an Iowa Tall-Tower Network, J. Appl. Meteorol. Climatol., 53(10), 2387–2393, doi:10.1175/JAMC-D-13-0340.1, 2014.

Wilks, D. S.: Statistical methods in the atmospheric sciences, Academic Press., 2011.

Evaluation of the wind farm parameterization in the Weather Research and Forecasting model (version 3.8.1) with meteorological and turbine power data

Joseph C. Y. Lee and Julie K. Lundquist[1,2]
[1]Department of Atmospheric and Oceanic Sciences, University of Colorado, UCB 311, Boulder, CO 80309, USA
[2]National Renewable Energy Laboratory, Golden, CO, USA

Correspondence to: Joseph C. Y. Lee (chle6805@coloardo.edu)

Abstract. Forecasts of wind power production are necessary to facilitate the integration of wind energy into power grids, and these forecasts should incorporate the impact of wind turbine wakes. This paper focuses on a case study of four diurnal cycles with significant power production, and assesses the skill of the wind farm parameterization (WFP) ~~in~~distributed with the Weather Research and Forecasting (WRF) model version 3.8.1, as well as its sensitivity to model configuration. After validating the simulated ambient flow with observations, we quantify the value of the WFP as it accounts for wake impacts on power production of downwind turbines. We also illustrate that a vertical grid with nominally 12-m vertical resolution is necessary for reproducing the observed power production, with statistical significance. Further, the WFP overestimates wake effects and hence underestimates downwind power production during high wind speed and low turbulence conditions. We also find the WFP performance is independent of atmospheric stability, the number of wind turbines per model grid cell, and the upwind-downwind position of turbines. Rather, the ability of the WFP to predict power production is most dependent on the skill of the WRF model in simulating the ambient wind speed.

1 Introduction

In recent years, numerical weather prediction (NWP) models have become an indispensable tool in the wind energy industry, not only in day-to-day wind energy production forecasts (Wilczak et al., 2015), but also to support wide-scale wind power penetration (Marquis et al., 2011) and wind resource assessment. To forecast power production accurately at wind farms, the simulation tools should resolve all physical processes relevant to the wind field, including possible impacts of the wind turbines themselves. Consequently, including the effects of wind farms in NWP models can improve power production forecasts.

Researchers have developed various methods to numerically represent wind farms. Via large-eddy simulations (LES), some investigators assess the meteorological impacts of wind turbines as well as power production (Abkar and Porté-Agel, 2015b; Aitken et al., 2014; Calaf et al., 2010; Churchfield et al., 2012; Jimenez et al., 2007; Mirocha et al., 2014; Na et al., 2016; Sharma et al., 2016; Wu and Porté-Agel, 2011). Simulating wind turbines and their effects in LES is, while useful, computationally expensive, making wind-farm-scale simulations unreasonable in an operational setting.

At coarser spatial scales, suitable for global, synoptic or mesoscale models, numerically representing wind turbine effects ~~in~~ may involve unrealistic assumptions. For example, researchers have used exaggerated surface roughness to represent the wind speed (WS) reduction caused by wind farms in a global model (Barrie and Kirk-Davidoff, 2010; Frandsen et al., 2009; Keith et al., 2004). Similarly, the analytical wind park model of Emeis and Frandsen (1993) considers both the downward momentum flux and the momentum loss due to surface roughness. The revised model by Emeis (2010) accounts for the spatially-averaged momentum-extraction coefficient by turbines, and the parameters become atmospheric-stability dependent. However, these models omit the consideration of turbine-scale interactions between the hub and the surface (Abkar and Porté-Agel, 2015a; Fitch et al., 2012, 2013b).

Aside from indirectly representing wind turbines via exaggerated roughness, another common approach is to use the turbine power curve to deduce elevated drag and turbulence production of wind turbines. A power curve illustrates the relationship between inflow WS at hub height and power production of a particular turbine model. This method can model meteorological impacts of wind turbines and the impact of turbine drag force (Baidya Roy, 2011; Blahak et al., 2010). Based on this technique, Fitch et al. (2012) added the consideration of the turbine thrust coefficient to simulate both turbine drag and power loss.

In the wind farm parameterization (WFP) of the Weather Research and Forecasting (WRF) model, wind turbines in each model grid cell are collectively represented as a turbulence source and a momentum sink within the vertical levels of the turbine rotor disk (Fitch et al., 2012). A fraction of the kinetic energy extracted by the virtual wind turbines is converted to power, and the turbulence generation is derived from the difference between the thrust and power coefficients. In the WFP scheme, the use of the WS-dependent thrust coefficients accounts for the effects of local wind drag on wind energy extraction as well as on power estimation. The WRF WFP offers flexibility, where users can modify the parameters of a turbine model, such as its hub height, rotor diameter, power curve and thrust coefficients, and does not require other empirically-derived parameters. By simulating wind farms in a mesoscale weather model, WRF users can simulate aggregated effects of wind turbine wakes and thus the effects of power production of downwind turbines.

An approach similar to the WRF WFP proposed by Abkar and Porté-Agel (2015a), relies on an extra parameter, the ratio of the freestream velocity to the ~~horizontal~~ horizontally-averaged hub-height velocity of a turbine-containing grid cell. This ratio depends on various factors such as the wind farm density and layout, and requires preliminary simulation results (Abkar and Porté-Agel, 2015a). Therefore, the publicly-available WFP in the WRF model is chosen in this project for observed power comparison. On the other hand, the explicit wake parameterization (~~WEP~~EWP) recently designed by Volker et al. (2015) uses classical wake theory to describe the unresolved wake expansion. Both the WRF WFP and the ~~WEP~~EWP average the drag force within grid cells. Nevertheless, users of the ~~WEP~~EWP need to adjust the length scales that determine wake expansion in the ~~WEP~~EWP for different situations.

In this paper, we evaluate the WFP in the WRF model via comparison to turbine power production data. The WRF WFP has been widely used to assess the impacts, of both onshore and offshore wind farms, at different spatial scales, and in different stability regimes (Eriksson et al., 2015; Fitch et al., 2013a, 2013b; Jiménez et al., 2015; Lee and Lundquist, 2017; Miller et al., 2015; Vanderwende et al., 2016; Vanderwende and Lundquist, 2016; Vautard et al., 2014). While WFP predictions have been compared to power production in offshore wind farms for a limited set of wind speeds (Jiménez et al., 2015), here we explore a range of WS, wind direction (WD), turbulence, and atmospheric stability conditions. The large range of wind conditions induces spatially- and temporally-diverse power production, thereby providing a basis for a comprehensive evaluation of the WFP. The uniqueness of this project lies in the in-depth assessment of the WRF WFP performance in forecasting and simulating wind energy of a sizable onshore wind farm, using observed power production data.

We describe the observation data and the model design in Section 2. In Section 3, we evaluate the simulations by comparison to meteorological and power generation data. We close with a statistical examination and a proposal of improvements on the WRF WFP in Section 4.

2 Data and Methods

2.1 Observations

The 2013 Crop Wind Energy eXperiment (CWEX-13) took place in central Iowa at a 200-turbine wind farm to quantify far-wake impacts of multiple rows of turbines (Lundquist et al., 2014). In CWEX-13, measurements from seven surface flux stations, a radiometer, three profiling lidars and a scanning lidar were collected. This campaign was a component of the larger CWEX project, which explored the interactions of wind turbines with crops, surface fluxes and near-surface flows in different atmospheric stability regimes in flat terrain (Rajewski et al., 2013). Research facilitated by the CWEX projects include: diurnal changes in observed turbine wakes (Rhodes and Lundquist, 2013), turbine interactions with moisture and carbon dioxide fluxes (Rajewski et al., 2014), LES modelling of turbine wakes in changing stability regimes (Mirocha et al., 2015), nocturnal low-level jet (LLJ) occurrences (Vanderwende et al., 2015), diurnal changes of the microclimate near wind turbines (Rajewski et al., 2016), multiple-wake interactions (Bodini et al., 2017), the evolution of turbine wakes during the evening transition (Lee and Lundquist, 2017) and coupled mesoscale-microscale modelling (Muñoz-Esparza et al., 2017).

This wind farm consists of 200 wind turbines, represented by the red dots in Fig. 1. Half of the wind turbines in the wind farm are General Electric (GE) 1.5-MW super-long extended (SLE) model, and the other half are GE 1.5-MW extra-long extended (XLE) model (Rajewski et al., 2013). The cut-in and cut-out speeds of the SLE model are 3.5 and 25 m s^{-1} respectively, and the rated speed is 14 m s^{-1}. The XLE model has lower rated and cut-out wind speeds, at 11.5 and 20 m s^{-1}. The hub height of both models is 80 m; the rotor diameters of the SLE and the XLE model are 77 and 82.5 m respectively. For simplicity, references to the rotor diameter (D) herein refer to the 77-m rotor diameter. Power generated by each turbine is recorded by the Supervisory Control and Data Acquisition (SCADA) system every 10 minutes, and we sum up the power production of all turbines for wind-farm production for each 10-min period.

Observations of the wind profile are collected by a profiling lidar and a scanning lidar. The WINDCUBE v1 (WC) profiling lidar (yellow square in Fig. 1), is located 528 m, or 6.3 D, south of the nearest turbine. The WC lidar measures winds at about 0.25 Hz from 40 to 220 m above ground level (AGL) every 20 m via the Doppler beam swinging (DBS) method. The WC lidar derives wind components by measuring radial velocities using Doppler beam swinging at an azimuth angle of 28°. Note that the WC-observed turbulence parameters, turbulence kinetic energy (TKE) and turbulence intensity (TI), are derived from the variances of the three wind components in two-min intervals, hence not representing small-scale turbulence. The turbulence parameters are defined by:

$$TKE = \frac{1}{2}(\sigma_u^2 + \sigma_v^2 + \sigma_w^2), \qquad (1)$$

$$TI = \frac{\sqrt{\sigma_u^2 + \sigma_v^2}}{\overline{U}}, \qquad (2)$$

where σ^2 are the 2-min averaged variances of the u, v, and w wind components, and $\overline{U}$ is the mean horizontal WS (Stull, 1988). In CWEX-11, wind turbine wake measurements at a different location in this wind farm were collected with these instruments (Rhodes and Lundquist 2013), while the error in these lidar measurements due to inhomogeneous flow were explored by Bingöl et al. (2009) and Lundquist et al. (2015).

The WINDCUBE 200S scanning lidar (green square in Fig. 1), is positioned 437 m, or 5.7 D, north of the nearest turbine row. The 200S lidar scanning strategy included velocity azimuth display (VAD) scans that measures winds from $\sim$ 100 to $\sim$~~-~~4800 m AGL nominally every 50 m for every 3 minutes. We use the 200S 75-degree-elevation scans (Vanderwende et al., 2015) to estimate horizontal winds every 30 minutes to verify the simulated winds in the boundary layer. Since the dominant wind directions during the campaign are south-easterly to south-westerly (Vanderwende et al., 2015), some of the 200S measurements below the rotor top (about 120 m AGL) could be influenced by turbine wakes during conditions, in which wakes persist longer than 5 D downwind from the turbine (Bodini et al., 2017). On the other hand, WC measurements are largely unaffected by turbine wakes except when WD is east of 150°. The closest upwind turbine during this simulation period was located over 2.7 km (33 D) to the southeast.

Surface flux station measurements can also quantify model skill. The surface flux station of interest (purple square in Fig. 1), is located 681 m, or 8.8 D, south of the closest turbine. At 8 m AGL, the station measures 20-Hz winds via a CSAT3 sonic anemometer, as well as virtual temperature and water vapour density via a HMP45C probe. After tilt-correction (Wilczak et al., 2001), we calculate surface sensible heat flux using a 30-min averaging time period. The Ob~~h~~ukhov length (L) categorizes atmospheric stability conditions:

$$L = -\frac{\overline{T_v} u_*^3}{k g (\overline{w' T_v'})_s}, \qquad (3)$$

where $\overline{T_v}$ is the mean virtual temperature, u_* is the frictional velocity, k is the von Karman constant, g is the gravity acceleration, and $(\overline{w' T_v'})_s$ is the surface virtual temperature flux calculated from the 20-Hz measurements (Stull, 1988). ~~A~~

~~p~~Positive surface sensible heat flux and Obukhov Length ratio ($z\ L^{-1}$), where z is 8 m, indicate~~s~~ a stable atmosphere, while ~~a~~ negative values indicates unstable conditions.

From 24-27 August 2013, nocturnal LLJs were observed (Vanderwende et al., 2015). No major synoptic events affected the area during this period. Moreover, when the near-surface flows are southerly, the WC and the surface flux station measure winds unaffected by the presence of wind turbines (Muñoz-Esparza et al., 2017). Additionally, no curtailment of the wind turbines occurred and the instruments operated normally during the period, making these four days ideal for model verification.

2.2 Modelling

To establish direct comparison with the observations, we simulate winds with and without the wind farm parameterization (WFP) using the Advanced Research WRF model (version 3.8.1) (Skamarock and Klemp, 2008). We simulate the winds on each day separately, from 0 UTC to 0 UTC, after 12 h of spin-up time. The ERA-interim (Dee et al., 2011) and the 0.5° Global Forecast System (GFS) reanalysis datasets provide boundary conditions for two different sets of model runs. We set three domains in our simulations with horizontal resolutions of 9, 3 and 1 km respectively, where the finest domain covers the state of Iowa (Fig. 1). To capture the westerly synoptic flow and the southerly near-surface winds, we position the inner grids northeast of the centres of the coarser grids.

The WFP scheme simulates wind farms and their meteorological influences to the atmosphere. We provide a brief summary here, and the details are discussed in Fitch et al. (2012). Wind turbines slow down ambient wind flow and convert a part of the kinetic energy of wind into electrical energy. The WFP represents this wind-turbine drag force as the kinetic energy harvested by the turbine from the atmosphere:

$$\boldsymbol{F}_{drag} = \frac{1}{2} C_T(|\boldsymbol{V}|)\rho|\boldsymbol{V}|A\boldsymbol{V},$$

where C_T is the turbine-specific thrust coefficient (discussed in detail in Fitch, 2015), $\boldsymbol{V}$ is the horizontal velocity vector, ρ is air density, $A = \frac{\pi}{4}D^2$ and is the cross-sectional rotor area, and D is the rotor diameter. This kinetic-energy extraction also causes changes in the atmosphere, namely the kinetic energy loss in the grid cell, which is described by the momentum tendency:

$$\frac{\partial|\boldsymbol{V}|_{ijk}}{\partial t} = \frac{N_t^{ij} C_T(|\boldsymbol{V}|_{ijk})|\boldsymbol{V}|_{ijk}^2 A_{ijk}}{2(z_{k+1}-z_k)},$$

where i, j, and k represents the zonal, meridional, and vertical grid indices, N_t^{ij} is the number of wind turbines per square meter, and z_k is the height at model level k. Of the kinetic energy extracted by the turbines, the WFP accounts for the electricity generation with:

$$\frac{\partial P_{ijk}}{\partial t} = \frac{N_t^{ij} C_P(|\boldsymbol{V}|_{ijk})|\boldsymbol{V}|_{ijk}^3 A_{ijk}}{2(z_{k+1}-z_k)},$$

where P_{ijk} is the power output in the grid cell in Watts, and C_P is the power coefficient. Assuming negligible mechanical and electrical losses, the rest of the kinetic energy harvested turns into TKE:

$$\frac{\partial TKE_{ijk}}{\partial t} = \frac{N_t^{ij} C_{TKE}(|\boldsymbol{V}|_{ijk})|\boldsymbol{V}|_{ijk}^3 A_{ijk}}{2(z_{k+1}-z_k)},$$

where TKE_{ijk} is the TKE in the grid cell, and C_{TKE} is the difference between C_T and C_P.

We employ two resolutions of vertical grids: nominally 12 m and 22 m resolution below 400 m above the surface, with 80 and 70 total levels respectively (Fig. 2). Three and six vertical levels intersect the atmosphere below and within the rotor layer in the finer vertical grid, while the 22-m grid only allows one full level below and four levels within the rotor layer. The vertical levels are further stretched beyond the boundary layer. In past research involving the WRF WFP, the selections of vertical resolution within the rotor layer include: 9 to 18 m in Vanderwende et al. (2016); about 10 to 16 m in Volker et al. (2015); about 15 m in Fitch et al. (2012), Fitch et al. (2013a), Fitch et al. (2013b) and Vanderwende and Lundquist (2016); about 20 m in Miller et al. (2015) and Vautard et al. (2014); about 22 m in Lee and Lundquist (2017); about 40 m in Eriksson et al. (2015) and Jiménez et al. (2015).

The Mellor-Yamada-Nakanishi-Niino (MYNN) Level 2.5 Planetary Boundary Layer (PBL) scheme is currently required for use with the WFP ~~in~~distributed with the WRF model version 3.8.1 (Fitch et al., 2012). Note that substantial upgrades were made on the MYNN PBL schemes in WRF version 3.8 (WRF-ARW, 2016). The MYNN PBL scheme supports TKE advection, active coupling to radiation, cloud mixing from Ito et al. (2015) and mixing of scalar fields. The MYNN scheme also uses the cloud probability density function from Chaboureau and Bechtold (2002), and we keep the mass-flux scheme deactivated. We summarize the other configuration details in Table 1.

After verifying the background flow simulated by the WRF model (first 4 rows in Table 2), virtual turbines are added via the WFP (last 4 rows in Table 2). We simulate all the turbines using the 1.5-MW PSU generic turbine model (Schmitz, 2012), in which its specifications are based on the GE 1.5-MW SLE model installed at the wind farm. The turbines within the WRF grid cells are located with the latitudes and longitudes provided by the wind-farm owner-operator. The model grid cells within the wind farm, containing 1 to 4 wind turbines per cell, are labelled as blue numbers in Fig. 1. With the WFP activated, the model simulates the total power at each time step in each turbine-containing grid cell, regardless of the number of turbines per cell. To match the 10-min average power data from the turbines, we sample 10-min power from the WFP output.

We also estimate the power generation of the WRF simulations without using the WFP. Based on the ambient WS of the turbine-containing grid cells in the control WRF runs, we use the turbine power curve to obtain an assessment of the power every ten minutes. We then multiply the power with the number of turbines per cell to yield the appropriate power estimate in each grid cell, just as would be done in wind energy forecasting without a wake parameterization. This method of power estimation omits wake effects, in contrast to the WFP.

3 Results

3.1 Ambient Flow Evaluation

The WRF model simulations without the WFP simulate accurate ambient winds as compared to the lidar measurements. Qualitatively, the ERA12 simulation (see Table 2 for a listing of all the simulations), has skill in simulating WS and WD during the 4-day period, including the occurrence, the strength and the elevation of the nocturnal ~~low-level jets~~LLJs (Fig. 3). The 200S records the vertical shear caused by LLJs above 100 m (Fig. 3a), and the WC measures the near-surface winds with high temporal resolution (Fig. 3b). In both the observations and the simulations of WS (Fig. 3c), the night-time WS profile is stratified and the daytime atmosphere is well-mixed. The WD simulations also match well with the measurements, where in the evening the winds veer, or turn clockwise with height (Fig. 4), while the daytime flow shows relatively constant wind direction with height. Except for the last hours on 24 August, the ERA12 captures the general temporal and vertical fluctuations in WS and WD, as the winds changed from south-easterly to south-westerly (Fig. 3 and 4). The 200S measurements above the rotor layer (120 m) are unaffected by turbine wakes (Fig. 3a and Fig. 4a); the LLJs observed above the rotor layer resemble those from the ERA12, supporting the skills of the simulations. To evaluate the effects of boundary conditions and vertical resolutions on simulating winds, we compare the 4 no-WFP runs: ERA12, ERA22, GFS12 and GFS22.

Quantitatively, simulations using finer vertical resolution have more skill in simulating winds than those with coarser resolution (Table 3). In comparison to the 200S and WC observations, the mean absolute errors in WS and WD of the 12-m runs are lower than those of the 22-m runs over the 4-day period, by 0.3 m s^{-1} and 0.8° in average. Particularly in the ERA12, the errors in WS decrease by at least 19% relative to the ERA22. Although the GFS22 yields smaller WS errors than the ERA22, refining the vertical grid of the simulations of either boundary condition dataset improves the skill of the WRF model more than changing the boundary conditions (Table 3). The errors in simulating WD remain similar regardless of the choice of boundary condition or vertical grid. Of all our control runs, the ERA12 simulates the most accurate inflow.

3.2 Power Simulations

The simulation omitting the WFP ignores the wake effects on downwind turbine power production, and therefore overestimates total power. For each 10-min time step, we compare the spatial distribution of power production as well as the total power between the ERA12, the ERA12WF, and the observations; Fig. 5 represents one 10-min time step in the 4-day period. As mentioned above, we calculate the power estimates of ERA12 using the ambient WS and the number of turbines in each grid cell as well as the power curve (Fig. 5a). The WRF WFP generates power predictions (Fig. 5b), and we sum up the observed power production in each grid cell (Fig. 5c). We present the total 10-min observed and simulated power of the whole wind farm at the bottom of each panel in Fig. 5~~.~~, where the total power production of the WFP run matches the observed. We then compile the 576 10-min total power values over the 4-day period and compare the simulations to the observations (Fig. 6). We also calculate an error and a bias of modelled total power for each 10-min interval, summarizing as the daily root-mean-squared errors (RMSE) and average biases in Table 4 and 5. The large average biases in Table 5 highlight the consistent power overestimation of the no-WFP runs.

Over the 4-day period, the WFP produces total power of the whole wind farm that generally agrees with observation (Fig. 6c). Although the RMSEs between the no-WFP and WFP runs are comparable (Table 4), the average biases are smaller in the WFP simulations (Table 5). For example, the ERA12WF slightly under-predicts total power by -4.9 MW on average (Fig. 6c and Table 5). The ERA12, by contrast, consistently over-predicts power production by 41.5 MW (Fig. 6a and Table 5). The daily positive biases of the ERA12 in the first 2 days are nearly 20% of maximum wind farm production (Table 5). The average positive power bias of 36.2 MW in the ERA22 is also remarkably larger than the mild negative bias of -15.1 MW in the ERA22WF (Fig. 6b and d, Table 5). Furthermore, the ERA12 and the GFS12 generally outperform the ERA22 and the GFS22 in power predictions, particularly in RMSE (Fig. 6 and Table 5). However, on the last day, with more south-westerly flow, the ERA12 and the ERA22 outperform the ERA12WF and the ERA22WF, while the GFS12WF and the GFS22WF yield smaller errors and biases (Table 4 and 5). Nonetheless, in aggregate, the simulations using the WFP predict wind-farm power production with more skill than simulations without the WFP.

As demonstrated by the average absolute errors (Table 3), the WFP power simulations improve when using 12-m rather than 22-m vertical resolution (Fig. 6). Changing the vertical grid improves the predictions more than changing boundary conditions (Table 4 and 5). Particularly in the ERA-interim simulations, the RMSE each day decreases by 19% to 39% when switching from ERA22WF to ERA12WF, also seen in Fig. 6c and d. Since the power prediction skills of the ERA-interim-initiated runs and the GFS-initiated runs are comparable, the rest of the paper will focus on the WFP runs using the ERA-interim initial and boundary conditions.

Moreover, to statistically differentiate the power productions from various model runs, we apply the 2-sample Student's t-test. The null hypothesis of a 2-sample t-test is that the two population means are the same, assuming the underlying distributions are Gaussian (Wilks, 2011). Hence, if the resultant p-value is equal to or below 0.05, the two distributions are statically significantly different at the 95% confidence level. For example, the difference between the 4-day power-production averages from the ERA12 and from the ERA12WF is -46.8 MW. The respective p-value is 0, thus the difference of the means is statistically significant (Table 6). In other words, the ERA12 and the ERA12WF yield different power production distributions. Similarly, the GFS12 and the GFS12WF lead to statistically different power outputs as the p-value from t-test is 0 as well (Table 7). We also use the 2-sample t-test to contrast the actual and the modelled power distributions. For instance, all the p-values between the no-WFP runs and the observation are 0, implying those simulations yield power distributions significantly different from the reality (Table 8).

Given the utility of the WFP, assessing the interactions between atmospheric forcing and power is an important step to further examine the performance of the WFP. As with the ERA12, the ERA12WF adequately simulates the evolution of the meteorological variables over the 4-day period (Fig. 7a to ~~c~~d). Both the ERA12 and the ERA12WF capture the overall trends of hub-height ambient WS and WD measured by the WC (Fig. 7a and b), corresponding to Fig. 3 and 4. On the other hand, although the simulations suggest stronger TKE diurnal cycles than the observations, especially in the first 36 h, the simulated values follow the trends of the WC-measured TKE (Fig. 7c). Although the magnitudes of the surface sensible heat flux of the surface flux station and the simulations differ, their signs change at similar times, particularly in the last three days (Fig. 7d). Hence the WRF model is capable to represent diurnal atmospheric stability changes. Note that in Fig. 7c, the lidar derives TKE using 2-min variances, which is intrinsically different from the modelled TKE, as discussed in Kumer et al. (2016) and Rhodes and Lundquist (2013). Hence, readers should focus on the general trends of the TKE time series, rather than their absolute values.

The observed WS fluctuates more than the mesoscale simulated WS during daytime (Fig. 7a). The ramp events, where the WS increases rapidly in a short period (Kamath, 2010; Potter et al., 2009), induce considerable increases in observed power (Fig. 7~~d~~e). The five distinct ramp events are from 00 to 01 UTC on 24 August, from 18 to 19 UTC 24 August, from 00 to 01 UTC 25 August, from 00 to 02 UTC 26 August, and from 00 to 02 UTC 27 August. Most of the ramp events are related to the LLJs (Fig. 3), and the simulated WS usually lags that observed (Fig. 7a). Therefore, the WFP under-predicts total power in nearly all the ramp events (Fig. 7~~d~~e). Note that the measured WS ranges between the cut-in and rated speed of the wind turbine, a range in which the power is highly sensitive to WS. The strong linkage between the temporal fluctuations of WS and power emphasizes the importance of accurate WS predictions.

Along the same line, the WFP power performance changes in different meteorological conditions. To quantify WFP's skills, we use the bias in total power as a benchmark, calculated by subtracting the observed power from the WFP simulated power every 10 minutes (Fig. 8). Particularly in conditions of strong winds and weak turbulence, the WFP overestimates wake effects and thus underestimates power. On the other hand, for calm conditions with moderate or strong turbulence, the WFP tends to underestimate wake effects and thereby over-predicts power (Fig. 8a and c). The Pearson correlation coefficient between total power bias and WC-observed TKE is 0.48 (not shown).

On the contrary, WD and atmospheric stability have weaker influence on the skill of the WFP in general. The winds gradually rotate from south-easterly to south-westerly over this 4-day period while maintaining similar magnitudes of wind speed. During this direction shift, the WFP demonstrates a weak positive power bias when the WD is strictly southerly, while the biases skew negative when the winds have more easterly or westerly component (Fig. 8b). Similarly, the WFP power bias is unresponsive to stability changes, although strongly stable conditions tend to have low bias (Fig. 8d). ~~At the same time~~ S~~, s~~trongly stable conditions tend to have stronger and more distinct wakes (Abkar and Porté-Agel, 2015b; Lee and Lundquist, 2017; Magnusson and Smedman, 1994; Rhodes and Lundquist, 2013).

To isolate the WFP errors in power predictions from the WRF model errors in ambient wind simulations, we analyse a subset of data where the winds are simulated accurately. When the absolute error in wind speed is smaller than 1 m s^{-1} and the absolute error in wind direction is smaller than 5°, the relationships between power bias and WS, WD and TI (Fig. 9a to c) remain similar to the general trends shown in Fig. 8a to c. The WS-power-bias and TI-power-bias correlations become stronger in this subset (Fig 9a and c), compare with all the data in the 4-day period (Fig 8a and c). Moreover, when considering only cases of accurate wind predictions, the correlation between power bias and stability increases from -0.06 (Fig. 8d) to -0.42 (Fig. 9d). If the few strongest stability points (z L^{-1} larger than 0.55) are removed from the analysis, a weak negative correlation with stability emerges as the Pearson correlation coefficient becomes -0.61. Additionally, generally south to south-westerly flows yield stronger negative power biases.

As may be expected, when the model properly simulates ambient WS, the WFP performs better. When the ERA12WF predicts larger WS than observed, the simulation over-predicts the total power. The positive WFP power bias corresponds to WS overestimation, and the negative bias is associated with WS underestimation (Fig. 10). Interestingly, when the error in simulated total power lies between ±30 MW, the error of the simulated WS is mostly within ±2 m s^{-1}. On the other hand, the power bias does not seem to be related to wind direction or to ambient TKE: the correlation between the power bias and the simulated WD (TKE) bias is low, 0.3 (0.22) (not shown). Although the simulated WD and TKE generally match the WC observations (Fig. 7b and c), and the model's skills in simulating WD and TKE are relatively irrelevant to the WFP's power performance.

Although the WFP omits sub-grid-scale wake interactions between the wakes of multiple turbines within a cell, this omission does not affect the accuracy of the ERA12WF in power prediction: the performance of the WFP is insensitive to the number of turbines per model grid cell. The turbine-normalized bias demonstrates no dependence on the number of turbines within the model grid cell (Fig. 11). Each whisker in Fig. 11 marks the maximum, the upper quartile, the median, the lower quartile and the minimum of the average bias. Despite the large positive biases of the maxima, more than half of the average biases fall between ±1.5 MW, regardless of the numbers of turbines per cell (Fig. 11). Simulating 1 or 4 turbines in a grid cell (Fig. 1) does not influence the WFP's overall power prediction performance in the cases shown here.

Furthermore, the WFP performance remains consistent between upwind and downwind turbines, based on their positions against the ambient winds (Fig. 12). Given the square shape of grid cells, we determine the sequential rows of turbines during strictly southerly flows, with WD between 175° and 185° (Fig. 12a). The bulk of the normalized power biases fall within 0 to 0.4 MW, regardless of the upwind-downwind positions of turbines. Additionally, the power bias is independent of the mean distance between the actual turbine locations and the centre points of their respective grid cells (not shown).

4 Discussion

Herein, we compare WRF model simulations with different choices of vertical resolutions and boundary conditions. The evidence suggests that, at least for this onshore case with a strong diurnal cycle, the vertical resolution is more crucial than the choice of boundary conditions in simulating accurate winds and wind power production. Shin et al. (2011) have explored the impacts of the lowest model level on the performance of various PBL schemes in the WRF model, suggesting that increasing the number of model layers can simulate more accurately the surface layer in different stability regimes. In this study, we further illustrate that establishing more vertical levels in the boundary layer as well as the rotor layer improves the skills of the WRF model in simulating ambient WS, ambient WD and wind power (Table 3, 4 and 5). Furthermore, Carvalho et al. (2014) discussed the effects of different reanalysis datasets on wind energy production estimates and found the ERA-interim presents the most precise initial and boundary conditions, followed by the GFS. Herein, we test the ERA-interim and the 0.5° GFS, and both datasets produce simulations that resemble observed winds and power generations. Since the simulated power is sensitive to the resolution of model vertical grid, particularly near the surface, future WRF WFP users should select vertical levels with care.

Additionally, the outcomes from the statistical tests among the model runs further validate the importance of using the WFP as well as using a fine vertical grid. From the Student's t-test, the p-values of all the no-WFP and WFP pairs are 0 (Table 6 and 7), demonstrating that the differences between the distributions of the no-WFP runs and the WFP runs are statistically significant at any confidence level. Therefore, to accurately simulate power production, applying the WFP is better than not using it, regardless of the choice of vertical resolution and boundary condition, and the corresponding improvements in Table 4 and 5 are statistically significant. Although the distinction between the GFS12WF and GFS22WF is not statistically significant at the 90% confidence level (Table 7), switching from ERA22WF to ERA10WF improves power simulations significantly with 99% confidence (Table 6). In particular, the RMSE drops by 19.1 MW and the bias reduces by 10.2 MW in average in the ERA12WF (Table 4 and 5), and these are proven statistically significant.

Similarly, results from the statistical tests between the distributions of power from models and observations support the value of the WFP applied in a fine vertical grid. The p-values of the ERA12WF-observed pair and the GFS12WF-observed pair are 0.106 and 0.167 respectively (Table 8). The high p-values illustrate the distinctions between the distribution of observed power and the distributions of simulated power from the 12-m WFP simulations are not statistically significant, at the 90% confidence level. Among all the simulations analysed above, running the WFP over the 12-m vertical grid is the only combination that is not statistically different from observations (Table 8). In other words, the 12-m WFP simulations provide the closest approximations, of all the simulations, to the actual power production. Hence, the only way to predict wind-farm power production using the WRF model that is similar to (not statistically different from) observations is to use the WFP with 12-m resolution, regardless of the boundary condition dataset.

One of the objectives of this study is to propose general directions for improvements on the WFP. First of all, as the key determining factor in wind power production, WS plays a critical role. Ramp events pose a challenge to the WRF model in simulating WS as well as to the WFP in predicting power (Fig. 7a and ~~d~~e). On the other hand, wind speeds exceeding 10 m s^{-1}, although below rated speed, lead to WFP power underestimation (Fig. 8a). Furthermore, the WFP performance depends more on the horizontal winds and turbulence, rather than their vertical components, since the power bias correlates stronger with TI than TKE (Fig. 8c). Reducing turbulence diffusion in the WRF model could potentially yield more accurate simulated winds in stable conditions, including LLJs (Sandu et al., 2013); active research in modifying mixing lengths (Jahn et al., 2017) is suggesting promising results. More importantly, improving the skills of the WRF model in simulating WS can improve the WFP power performance (Fig. 10). Future versions of the WRF model as well as the WFP should aim to better account for instantaneous horizontal WS variations and the subsequent sub-gird wake interactions.

Besides necessary improvements in simulating ambient WS, the WFP scheme itself also requires refinements. When background winds are accurately predicted, the power-bias dependence on WS and TI remain strong (Fig. 9a and c).

Although the relationship between the WFP performance and stability is generally indistinct, the correlation becomes weakly negative without the strongly stable data. Even when the simulated winds are close to observations, the WFP underestimates power during high WS, south to south-westerly flow, low TI and stable conditions. Certainly the interactions between WD and wind-farm layout affect the power-bias relationships, while further sensitivity tests can further upgrade the WFP performance, particularly in intra-cell WS reduction. We demonstrate that inter-cell wake effects are not the critical factor to power error (Fig. 12b), hence the inability of the WFP to simulate intra-cell wake effects can explain the biases when many of the turbines experience accurately-simulated ambient flow.

In contrast, WD has no clear influence on the WFP skill (Fig. 8b) in this case, although the irregular shape of the wind farm adds uncertainty to this relationship. Similarly, the skill of the WFP for this case is insensitive to~~ atmospheric stability,~~ the number of virtual turbines per cell, and the downwind position of turbines against inflow (Figs.~~. 8d,~~ 11 and 12). Compared to the power overestimation of downwind turbines in the idealized cases described in Vanderwende et al. (2016), both the upwind and downwind turbine-containing cells presented in this study have consistent positive biases on power production (Fig. 12). Our findings suggest that the WFP is skilful in simulating power of aggregate wind turbines and can represent the impact of wakes between grids on power. In the end, the primary limitation of the WFP is rooted in the ambient simulated WS in the WRF model.

5 Conclusion

The WFP scheme in the WRF model (version 3.8.1) provides a convenient way to represent wind farms and their meteorological impacts in the NWP models. However, its power predictions have not been verified for onshore wind farms or in a range of wind speed conditions. Herein, we evaluate the performance of the WFP in a range of atmospheric conditions to guide users of the WFP and to suggest future WFP advancements.

Using data from the CWEX-13 campaign, we select a 4-day period, from 24 to 27 August 2013, for our case study, due to the consistent nocturnal ~~low-level jet~~LLJ occurrences. We use measurements from a profiling lidar, a scanning lidar and a surface flux station to verify the ambient flows simulated by the WRF model. The wind farm of interest, located in central Iowa, consists of 200 1.5 MW wind turbines.

We explore the role of vertical resolution in the operation of the WRF WFP. We evaluate two vertical grids with 12-m and 22-m resolution near the surface. We find that the finer vertical resolution produces simulations that agree better with observed WS, WD and power than simulations with coarser vertical resolution. Further, because the WFP accounts for the impacts of wakes on downwind turbine power production, the use of the WFP enables more accurate power prediction, whereas simulations without the WFP generally over-predict power production. Statically, the WFP simulations with a fine vertical grid, regardless of the boundary conditions, are the most skilful in simulating power.

The skill of the WFP varies with meteorological conditions. When the model simulates WS close to the observations, the WFP predicts power properly, making WS the critical factor in improving the WFP. Rapid temporal fluctuations in WS introduce errors in power simulations, especially during ramp events. Further, in windy and less turbulent conditions, the WFP tends to overestimate wake effects and thus underestimates power production. On the other hand, the WFP performance demonstrates no clear dependence on atmospheric stability, the number of turbines per model grid cell, or the downwind distance of turbines with respect to the upwind ones.

In conclusion, we demonstrate the value of the WRF WFP and the importance of using a fine vertical grid. Since WS greatly affects the skill of the WFP, subsequent research could include evaluating the WFP for an even larger range of WS, especially at wind speeds beyond the turbine cut-out speed (which would be 25 m s^{-1} in this case; no such high wind speeds were observed during the CWEX-13 campaign). Evaluating the performance of other wind farm layouts and in locations with complex terrain is also needed. Modifications in the inflow WS considered by the WFP, for example, considering the rotor equivalent wind speed (REWS) (Wagner et al., 2009), may bring promising improvements. More accurate power forecasts will shape a more competitive the wind energy industry, and further facilitate grid integration of wind energy (MacDonald et al., 2016).

Data Availability

The code of the WRF-ARW model (doi:10.5065/D6MK6B4K) is publicly available at http://www2.mmm.ucar.edu/wrf/users/download/get_source.html. This work uses the WRF-ARWmodel and the WRF Pre-Processing System (WPS) version 3.8.1 (released on 12 August, 2016), and the wind farm parameterization is distributed therein. The PSU generic 1.5 MW turbine (Schmitz, 2012) is available at doi:10.13140/RG.2.2.22492.18567. The user input (namelist) required to run the WRF WFP is available at doi:10.5281/zenodo.847780~~437166~~.

Acknowledgements

This study was funded by the National Science Foundation (Grant number: 1413980; Project Title: CNH-Ex: Legal, Economic, and Natural Science Analyses of Wind Plant Impacts and Interactions). The CWEX project was supported by the National Science Foundation under the State of Iowa EPSCoR Grant 1101284. The University of Colorado role in CWEX-13 was supported by the National Renewable Energy Laboratory. The authors thank the reviewers and editors for their thoughtful comments and suggestions. The authors would like to acknowledge high-performance computing support from Yellowstone (ark:/85065/d7wd3xhc) provided by NCAR's Computational and Information Systems Laboratory, sponsored by the National Science Foundation. The authors would also like to thank NextEra Energy for providing the wind turbine power data, Iowa State University for providing the surface flux measurements, and NRG Renewable Energy Systems and Leosphere for providing the 200S scanning lidar used in the CWEX-13 campaign.

References

Abkar, M. and Porté-Agel, F.: A new wind-farm parameterization for large-scale atmospheric models, J. Renew. Sustain. Energy, 7(1), 13121, doi:10.1063/1.4907600, 2015a.

Abkar, M. and Porté-Agel, F.: Influence of atmospheric stability on wind-turbine wakes: A large-eddy simulation study, Phys. Fluids, 27(3), 35104, doi:10.1063/1.4913695, 2015b.

Aitken, M. L., Kosović, B., Mirocha, J. D. and Lundquist, J. K.: Large eddy simulation of wind turbine wake dynamics in the stable boundary layer using the Weather Research and Forecasting Model, J. Renew. Sustain. Energy, 6(3), 33137, doi:10.1063/1.4885111, 2014.

Baidya Roy, S.: Simulating impacts of wind farms on local hydrometeorology, J. Wind Eng. Ind. Aerodyn., 99(4), 491–498, doi:10.1016/j.jweia.2010.12.013, 2011.

Barrie, D. B. and Kirk-Davidoff, D. B.: Weather response to a large wind turbine array, Atmos. Chem. Phys., 10(2), 769–775, doi:10.5194/acp-10-769-2010, 2010.

Bingöl, F., Mann, J. and Foussekis, D.: Conically scanning lidar error in complex terrain, Meteorol. Zeitschrift, 18(2), 189–195, doi:10.1127/0941-2948/2009/0368, 2009.

Blahak, U., Goretzki, B. and Meis, J.: A simple parametrisation of drag forces induced by large wind farms for numerical weather prediction models, in EWEC, pp. 186–189, Proceedings European Wind Energy Conference and Exhibition., 2010.

Bodini, N., Zardi, D. and Lundquist, J. K.: Three-Dimensional Structure of Wind Turbine Wakes as Measured by Scanning Lidar, Atmos. Meas. Tech. Discuss., 1–21, doi:10.5194/amt-2017-86, 2017.

Calaf, M., Meneveau, C. and Meyers, J.: Large eddy simulation study of fully developed wind-turbine array boundary layers, Phys. Fluids, 22(1), 15110, doi:10.1063/1.3291077, 2010.

Carvalho, D., Rocha, A., Gómez-Gesteira, M. and Silva Santos, C.: WRF wind simulation and wind energy production estimates forced by different reanalyses: Comparison with observed data for Portugal, Appl. Energy, 117, 116–126, doi:10.1016/j.apenergy.2013.12.001, 2014.

Chaboureau, J.-P. and Bechtold, P.: A Simple Cloud Parameterization Derived from Cloud Resolving Model Data: Diagnostic and Prognostic Applications, J. Atmos. Sci., 59(15), 2362–2372, doi:10.1175/1520-0469(2002)059<2362:ASCPDF>2.0.CO;2, 2002.

Chen, F. and Zhang, Y.: On the coupling strength between the land surface and the atmosphere: From viewpoint of surface exchange coefficients, Geophys. Res. Lett., 36(10), L10404, doi:10.1029/2009GL037980, 2009.

Churchfield, M. J., Lee, S., Michalakes, J. and Moriarty, P. J.: A numerical study of the effects of atmospheric and wake turbulence on wind turbine dynamics, J. Turbul., 13, N14, doi:10.1080/14685248.2012.668191, 2012.

Dee, D. P., Uppala, S. M., Simmons, A. J., Berrisford, P., Poli, P., Kobayashi, S., Andrae, U., Balmaseda, M. A., Balsamo, G., Bauer, P., Bechtold, P., Beljaars, A. C. M., van de Berg, L., Bidlot, J., Bormann, N., Delsol, C., Dragani, R., Fuentes, M., Geer, A. J., Haimberger, L., Healy, S. B., Hersbach, H., Hólm, E. V, Isaksen, L., Kållberg, P., Köhler, M., Matricardi, M., McNally, A. P., Monge-Sanz, B. M., Morcrette, J.-J., Park, B.-K., Peubey, C., de Rosnay, P., Tavolato, C., Thépaut, J.-N. and Vitart, F.: The ERA-Interim reanalysis: configuration and performance of the data assimilation system, Q. J. R. Meteorol. Soc., 137(656), 553–597, doi:10.1002/qj.828, 2011.

Ek, M. B., Mitchell, K. E., Lin, Y., Rogers, E., Grunmann, P., Koren, V., Gayno, G. and Tarpley, J. D.: Implementation of Noah land surface model advances in the National Centers for Environmental Prediction operational mesoscale Eta model, J. Geophys. Res., 108(D22), 8851, doi:10.1029/2002JD003296, 2003.

Emeis, S.: A simple analytical wind park model considering atmospheric stability, Wind Energy, 13(5), 459–469, doi:10.1002/we.367, 2010.

Emeis, S. and Frandsen, S.: Reduction of horizontal wind speed in a boundary layer with obstacles, Boundary-Layer Meteorol., 64(3), 297–305, doi:10.1007/BF00708968, 1993.

Eriksson, O., Lindvall, J., Breton, S.-P. and Ivanell, S.: Wake downstream of the Lillgrund wind farm - A Comparison between LES using the actuator disc method and a Wind farm Parametrization in WRF, J. Phys. Conf. Ser., 625(1), 12028, doi:10.1088/1742-6596/625/1/012028, 2015.

Fitch, A. C.: Notes on using the mesoscale wind farm parameterization of Fitch et al. (2012) in WRF, Wind Energy, 19, 1757–1758, doi:10.1002/we.1945, 2015.

Fitch, A. C., Olson, J. B., Lundquist, J. K., Dudhia, J., Gupta, A. K., Michalakes, J. and Barstad, I.: Local and Mesoscale Impacts of Wind Farms as Parameterized in a Mesoscale NWP Model, Mon. Weather Rev., 140(9), 3017–3038, doi:10.1175/MWR-D-11-00352.1, 2012.

Fitch, A. C., Lundquist, J. K. and Olson, J. B.: Mesoscale Influences of Wind Farms throughout a Diurnal Cycle, Mon. Weather Rev., 141(7), 2173–2198, doi:10.1175/MWR-D-12-00185.1, 2013a.

Fitch, A. C., Olson, J. B. and Lundquist, J. K.: Parameterization of Wind Farms in Climate Models, J. Clim., 26(17), 6439–6458, doi:10.1175/JCLI-D-12-00376.1, 2013b.

Frandsen, S. T., Jørgensen, H. E., Barthelmie, R., Rathmann, O., Badger, J., Hansen, K., Ott, S., Rethore, P.-E., Larsen, S. E. and Jensen, L. E.: The making of a second-generation wind farm efficiency model complex, Wind Energy, 12(5), 445–458, doi:10.1002/we.351, 2009.

Iacono, M. J., Delamere, J. S., Mlawer, E. J., Shephard, M. W., Clough, S. A. and Collins, W. D.: Radiative forcing by long-lived greenhouse gases: Calculations with the AER radiative transfer models, J. Geophys. Res. Atmos., 113(D13), D13103, doi:10.1029/2008JD009944, 2008.

Ito, J., Niino, H., Nakanishi, M. and Moeng, C.-H.: An Extension of the Mellor–Yamada Model to the Terra Incognita Zone for Dry Convective Mixed Layers in the Free Convection Regime, Boundary-Layer Meteorol., 157(1), 23–43, doi:10.1007/s10546-015-0045-5, 2015.

Jahn, D. E., Takle, E. S. and Gallus, W. A.: Improving Wind-Ramp Forecasts in the Stable Boundary Layer, Boundary-Layer Meteorol., 163, 423–446, doi:10.1007/s10546-017-0237-2, 2017.

Jimenez, A., Crespo, A., Migoya, E. and Garcia, J.: Advances in large-eddy simulation of a wind turbine wake, J. Phys.

Conf. Ser., 75(1), 12041, doi:10.1088/1742-6596/75/1/012041, 2007.

Jiménez, P. A., Navarro, J., Palomares, A. M. and Dudhia, J.: Mesoscale modeling of offshore wind turbine wakes at the wind farm resolving scale: a composite-based analysis with the Weather Research and Forecasting model over Horns Rev, Wind Energy, 18(3), 559–566, doi:10.1002/we.1708, 2015.

Kain, J. S.: The Kain–Fritsch Convective Parameterization: An Update, J. Appl. Meteorol., 43(1), 170–181, doi:10.1175/1520-0450(2004)043<0170:TKCPAU>2.0.CO;2, 2004.

Kamath, C.: Understanding wind ramp events through analysis of historical data, in IEEE PES T&D 2010, pp. 1–6, IEEE., 2010.

Keith, D. W., DeCarolis, J. F., Denkenberger, D. C., Lenschow, D. H., Malyshev, S. L., Pacala, S. and Rasch, P. J.: The influence of large-scale wind power on global climate, Proc. Natl. Acad. Sci. U. S. A., 101(46), 16115–16120, doi:10.1073/pnas.0406930101, 2004.

Kumer, V.-M., Reuder, J., Dorninger, M., Zauner, R. and Grubišić, V.: Turbulent kinetic energy estimates from profiling wind LiDAR measurements and their potential for wind energy applications, Renew. Energy, 99, 898–910, doi:10.1016/j.renene.2016.07.014, 2016.

Lee, J. C. Y. and Lundquist, J. K.: Observing and Simulating Wind-Turbine Wakes During the Evening Transition, Boundary-Layer Meteorol., 164(3), 449–474, doi:10.1007/s10546-017-0257-y, 2017.

Lundquist, J. K., Takle, E. S., Boquet, M., Kosović, B., Rhodes, M. E., Rajewski, D., Doorenbos, R., Irvin, S., Aitken, M. L., Friedrich, K., Quelet, P. T., Rana, J., Martin, C. S., Vanderwende, B. and Worsnop, R.: Lidar observations of interacting wind turbine wakes in an onshore wind farm, in EWEA. [online] Available from: http://www.leosphere.com/wp-content/uploads/2014/03/Lundquist_Boquet_EWEA_2014_CWEX13_final.pdf (Accessed 10 May 2017), 2014.

Lundquist, J. K., Churchfield, M. J., Lee, S. and Clifton, A.: Quantifying error of lidar and sodar Doppler beam swinging measurements of wind turbine wakes using computational fluid dynamics, Atmos. Meas. Tech., 8(2), 907–920, doi:10.5194/amt-8-907-2015, 2015.

MacDonald, A. E., Clack, C. T. M., Alexander, A., Dunbar, A., Wilczak, J. and Xie, Y.: Future cost-competitive electricity systems and their impact on US CO2 emissions, Nat. Clim. Chang., 6(5), 526–531, doi:10.1038/nclimate2921, 2016.

Magnusson, M. and Smedman, A. S.: Influence of atmospheric stability on wind turbine wakes, Wind Eng., 18(3), 139–152, 1994.

Marquis, M., Wilczak, J., Ahlstrom, M., Sharp, J., Stern, A., Smith, J. C. and Calvert, S.: Forecasting the Wind to Reach Significant Penetration Levels of Wind Energy, Bull. Am. Meteorol. Soc., 92(9), 1159–1171, doi:10.1175/2011BAMS3033.1, 2011.

Miller, L. M., Brunsell, N. A., Mechem, D. B., Gans, F., Monaghan, A. J., Vautard, R., Keith, D. W. and Kleidon, A.: Two methods for estimating limits to large-scale wind power generation, Proc. Natl. Acad. Sci., 112(36), 11169–11174, doi:10.1073/pnas.1408251112, 2015.

Mirocha, J. D., Kosovic, B., Aitken, M. L. and Lundquist, J. K.: Implementation of a generalized actuator disk wind turbine model into the weather research and forecasting model for large-eddy simulation applications, J. Renew. Sustain. Energy, 6(1), 13104, doi:10.1063/1.4861061, 2014.

Mirocha, J. D., Rajewski, D. A., Marjanovic, N., Lundquist, J. K., Kosović, B., Draxl, C. and Churchfield, M. J.: Investigating wind turbine impacts on near-wake flow using profiling lidar data and large-eddy simulations with an actuator disk model, J. Renew. Sustain. Energy, 7(4), 43143, doi:10.1063/1.4928873, 2015.

Muñoz-Esparza, D., Lundquist, J. K., Sauer, J. A., Kosović, B. and Linn, R. R.: Coupled mesoscale-LES modeling of a diurnal cycle during the CWEX-13 field campaign: From weather to boundary-layer eddies, J. Adv. Model. Earth Syst., doi:10.1002/2017MS000960, 2017.

Na, J. S., Koo, E., Muñoz-Esparza, D., Jin, E. K., Linn, R. and Lee, J. S.: Turbulent kinetics of a large wind farm and their impact in the neutral boundary layer, Energy, 95, 79–90, doi:10.1016/j.energy.2015.11.040, 2016.

Nakanishi, M. and Niino, H.: An Improved Mellor–Yamada Level-3 Model: Its Numerical Stability and Application to a Regional Prediction of Advection Fog, Boundary-Layer Meteorol., 119(2), 397–407, doi:10.1007/s10546-005-9030-8, 2006.

Potter, C. W., Grimit, E. and Nijssen, B.: Potential benefits of a dedicated probabilistic rapid ramp event forecast tool, in 2009 IEEE/PES Power Systems Conference and Exposition, pp. 1–5, IEEE., 2009.

Rajewski, D. A., Takle, E. S., Lundquist, J. K., Oncley, S., Prueger, J. H., Horst, T. W., Rhodes, M. E., Pfeiffer, R., Hatfield, J. L., Spoth, K. K. and Doorenbos, R. K.: Crop Wind Energy Experiment (CWEX): Observations of Surface-Layer, Boundary Layer, and Mesoscale Interactions with a Wind Farm, Bull. Am. Meteorol. Soc., 94(5), 655–672, doi:10.1175/BAMS-D-11-00240.1, 2013.

Rajewski, D. A., Takle, E. S., Lundquist, J. K., Prueger, J. H., Pfeiffer, R. L., Hatfield, J. L., Spoth, K. K. and Doorenbos, R. K.: Changes in fluxes of heat, H2O, and CO2 caused by a large wind farm, Agric. For. Meteorol., 194, 175–187, doi:10.1016/j.agrformet.2014.03.023, 2014.

Rajewski, D. A., Takle, E. S., Prueger, J. H. and Doorenbos, R. K.: Toward understanding the physical link between turbines and microclimate impacts from in situ measurements in a large wind farm, J. Geophys. Res. Atmos., 121(22), 2016JD025297, doi:10.1002/2016JD025297, 2016.

Rhodes, M. E. and Lundquist, J. K.: The Effect of Wind-Turbine Wakes on Summertime US Midwest Atmospheric Wind Profiles as Observed with Ground-Based Doppler Lidar, Boundary-Layer Meteorol., 149(1), 85–103, doi:10.1007/s10546-013-9834-x, 2013.

Sandu, I., Beljaars, A., Bechtold, P., Mauritsen, T. and Balsamo, G.: Why is it so difficult to represent stably stratified conditions in numerical weather prediction (NWP) models?, J. Adv. Model. Earth Syst., 5(2), 117–133, doi:10.1002/jame.20013, 2013.

Schmitz, S.: XTurb-PSU: A Wind Turbine Design and Analysis Tool, [online] Available from: http://www.aero.psu.edu/Faculty_Staff/schmitz/XTurb/XTurb.html, 2012.

Sharma, V., Calaf, M., Lehning, M. and Parlange, M. B.: Time-adaptive wind turbine model for an LES framework, Wind Energy, 19(5), 939–952, doi:10.1002/we.1877, 2016.

Shin, H. H., Hong, S.-Y. and Dudhia, J.: Impacts of the Lowest Model Level Height on the Performance of Planetary Boundary Layer Parameterizations, Mon. Weather Rev., 140(2), 664–682, doi:10.1175/MWR-D-11-00027.1, 2011.

Skamarock, W. C. and Klemp, J. B.: A time-split nonhydrostatic atmospheric model for weather research and forecasting applications, J. Comput. Phys., 227(7), 3465–3485, doi:10.1016/j.jcp.2007.01.037, 2008.

Stull, R. B.: An Introduction to Boundary Layer Meteorology, Springer., 1988.

Thompson, G. and Eidhammer, T.: A Study of Aerosol Impacts on Clouds and Precipitation Development in a Large Winter Cyclone, J. Atmos. Sci., 71(10), 3636–3658, doi:10.1175/JAS-D-13-0305.1, 2014.

Vanderwende, B. and Lundquist, J. K.: Could Crop Height Affect the Wind Resource at Agriculturally Productive Wind Farm Sites?, Boundary-Layer Meteorol., 158(3), 409–428, doi:10.1007/s10546-015-0102-0, 2016.

Vanderwende, B. J., Lundquist, J. K., Rhodes, M. E., Takle, E. S. and Irvin, S. L.: Observing and Simulating the Summertime Low-Level Jet in Central Iowa, Mon. Weather Rev., 143(6), 2319–2336, doi:10.1175/MWR-D-14-00325.1, 2015.

Vanderwende, B. J., Kosović, B., Lundquist, J. K. and Mirocha, J. D.: Simulating effects of a wind turbine array using LES and RANS, J. Adv. Model. Earth Syst., 8(3), 1376–1390, doi:10.1002/2016MS000652, 2016.

Vautard, R., Thais, F., Tobin, I., Bréon, F.-M., Lavergne, J.-G. D. de, Colette, A., Yiou, P. and Ruti, P. M.: Regional climate model simulations indicate limited climatic impacts by operational and planned European wind farms, Nat. Commun., 5, doi:10.1038/ncomms4196, 2014.

Volker, P. J. H., Badger, J., Hahmann, A. N. and Ott, S.: The Explicit Wake Parametrisation V1.0: a wind farm parametrisation in the mesoscale model WRF, Geosci. Model Dev., 8(11), 3715–3731, doi:10.5194/gmd-8-3715-2015, 2015.

Wagner, R., Antoniou, I., Pedersen, S. M., Courtney, M. S. and Jørgensen, H. E.: The influence of the wind speed profile on wind turbine performance measurements, Wind Energy, 12(4), 348–362, doi:10.1002/we.297, 2009.

Wilczak, J., Finley, C., Freedman, J., Cline, J., Bianco, L., Olson, J., Djalalova, I., Sheridan, L., Ahlstrom, M., Manobianco, J., Zack, J., Carley, J. R., Benjamin, S., Coulter, R., Berg, L. K., Mirocha, J., Clawson, K., Natenberg, E. and Marquis, M.: The Wind Forecast Improvement Project (WFIP): A Public–Private Partnership Addressing Wind Energy Forecast Needs, Bull. Am. Meteorol. Soc., 96(10), 1699–1718, doi:10.1175/BAMS-D-14-00107.1, 2015.

Wilczak, J. M., Oncley, S. P. and Stage, S. A.: Sonic Anemometer Tilt Correction Algorithms, Boundary-Layer Meteorol., 99(1), 127–150, doi:10.1023/A:1018966204465, 2001.

Wilks, D. S.: Statistical methods in the atmospheric sciences, Academic Press., 2011.

WRF-ARW: WRF Model Version 3.8: Updates, , doi:doi:10.5065/D6MK6B4K, 2016.

Wu, Y.-T. and Porté-Agel, F.: Large-Eddy Simulation of Wind-Turbine Wakes: Evaluation of Turbine Parametrisations, Boundary-Layer Meteorol., 138(3), 345–366, doi:10.1007/s10546-010-9569-x, 2011.

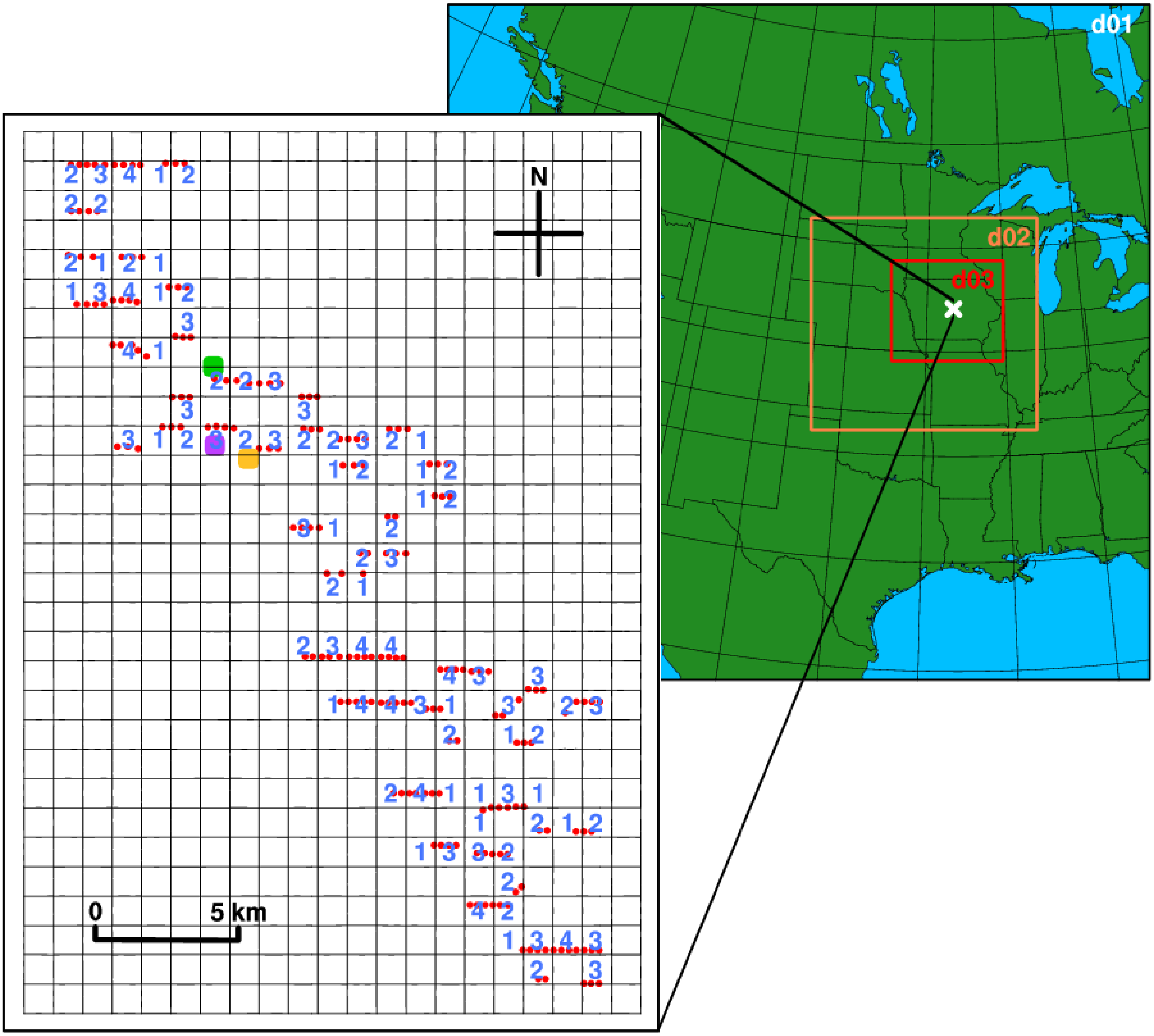

Figure 1: Map of the 3 domains (d01, d02 and d03) in the WRF simulations (right), with the white x representing the CWEX-13 wind farm. Zoom-in map of the wind farm (left), with the black horizontal and vertical lines outlining the WRF grid cells, the red dots as the actual locations of wind turbines, the blue numbers as the number of wind turbines per WRF grid cell, the yellow square as the WC lidar, the green square as the 200S lidar and the purple square as the surface flux station. Other instruments were deployed in CWEX-13, and only the instruments used herein are shown.

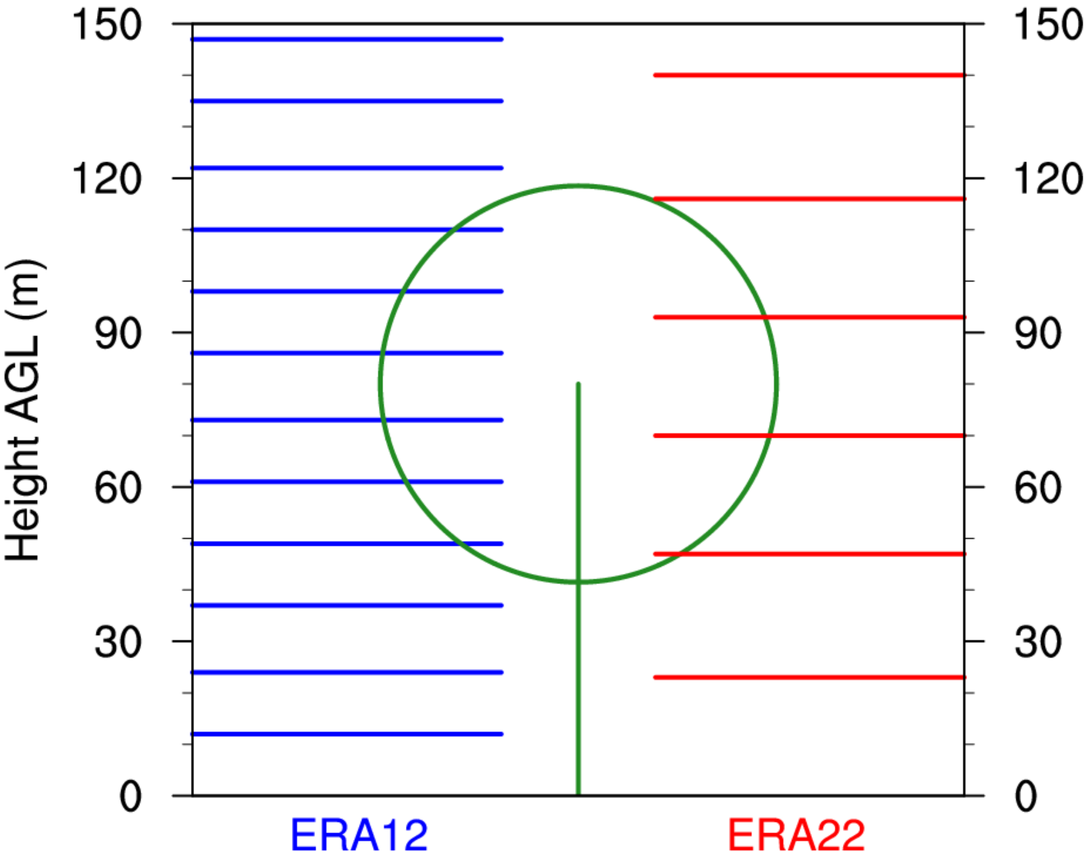

Figure 2: Illustration of the two vertical grids chosen: 12 m on the left in blue and 22 m on the right in red. Both grids shown use the ERA-interim as the boundary conditions. The simulations initiated with the 0.5° GFS have slightly different grids.

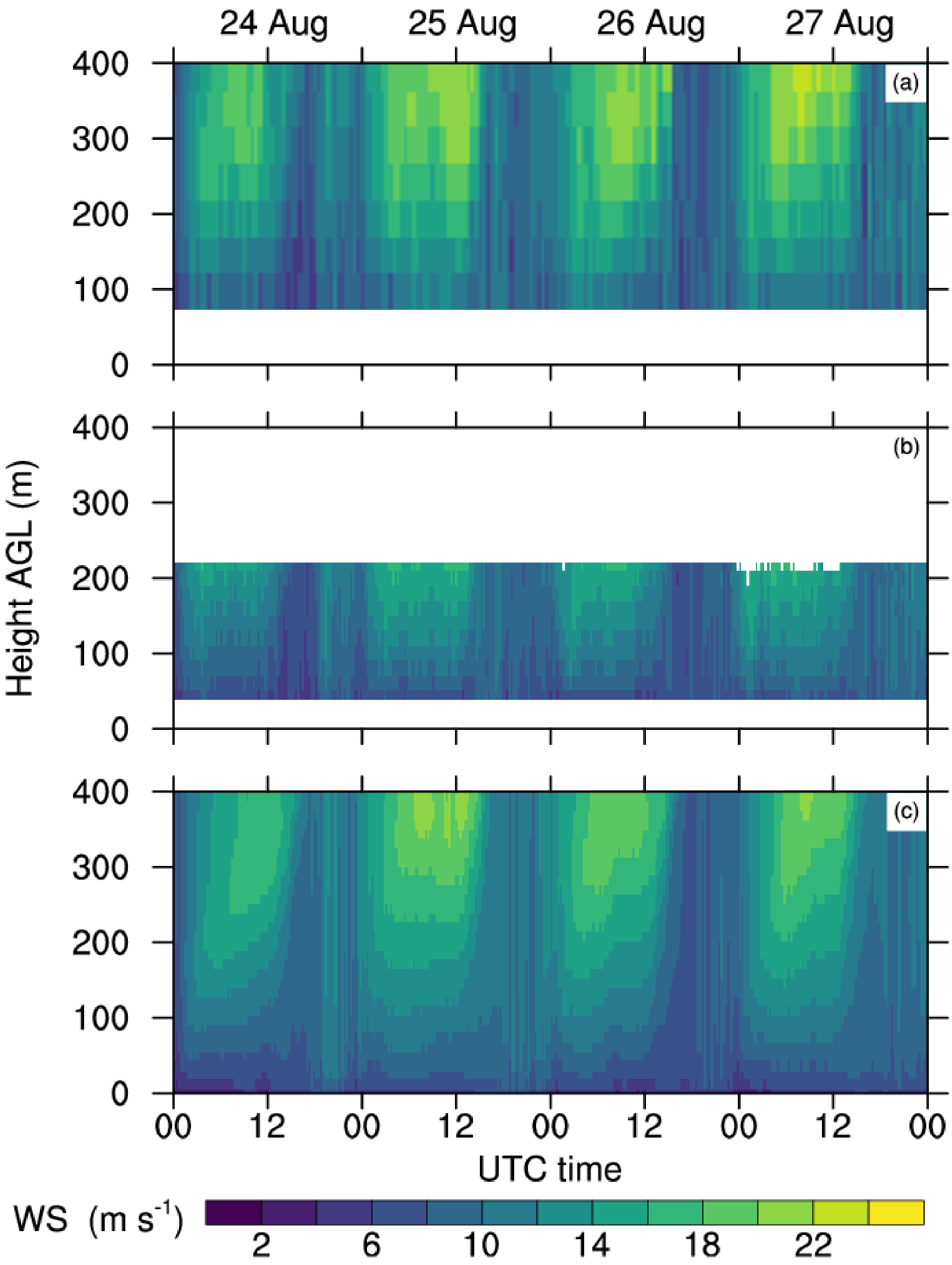
24 Aug
25 Aug
26 Aug
27 Aug
(a)
(b)
(c)
Height AGL (m)
400
300
200
100
0
00
12
UTC time
WS (m s^{-1})
2
6
10
14
18
22

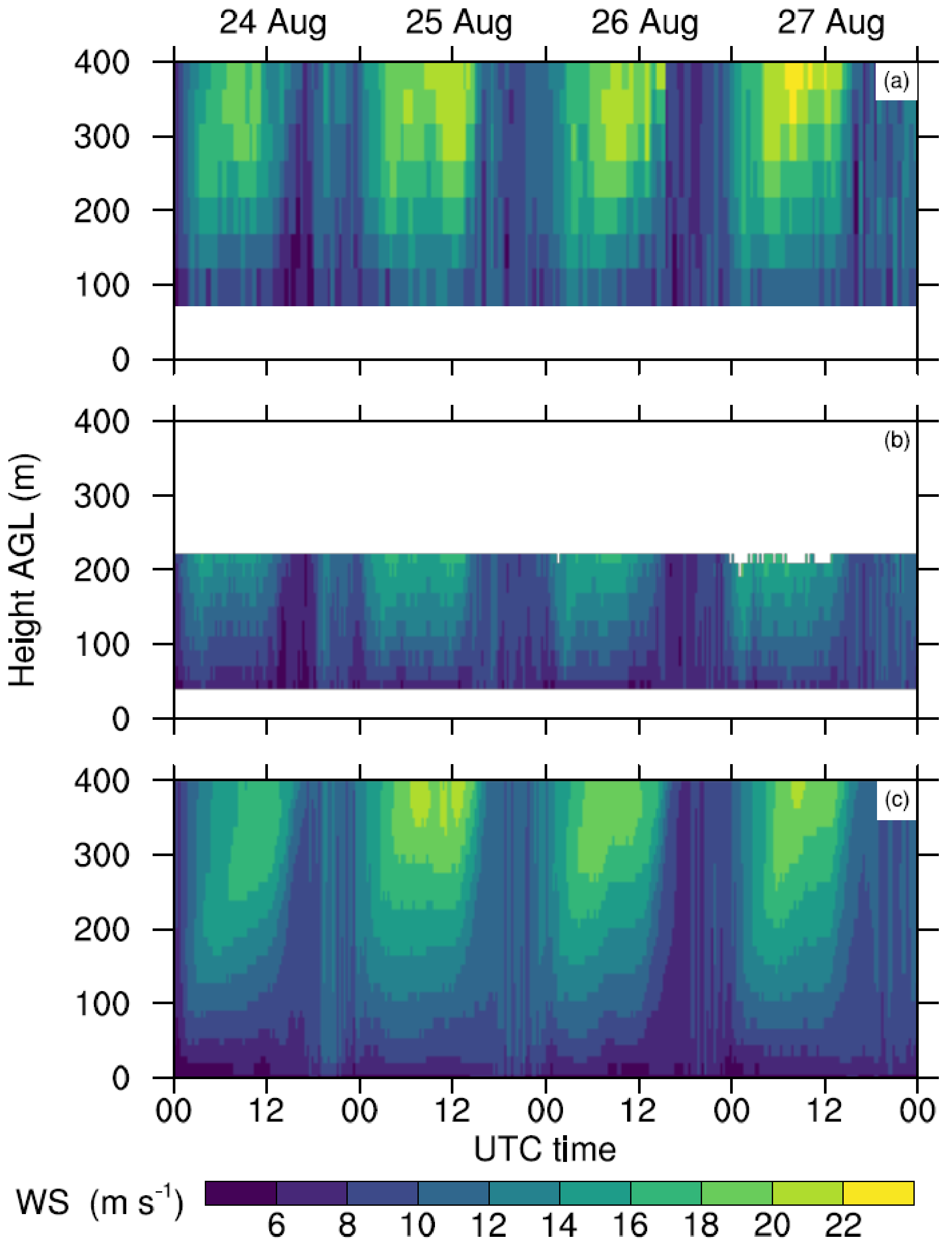

Figure 3: Time-height contour of WS from the 200S (a), the WC (b) and ERA12 at the closest grid point to the 200S (c).

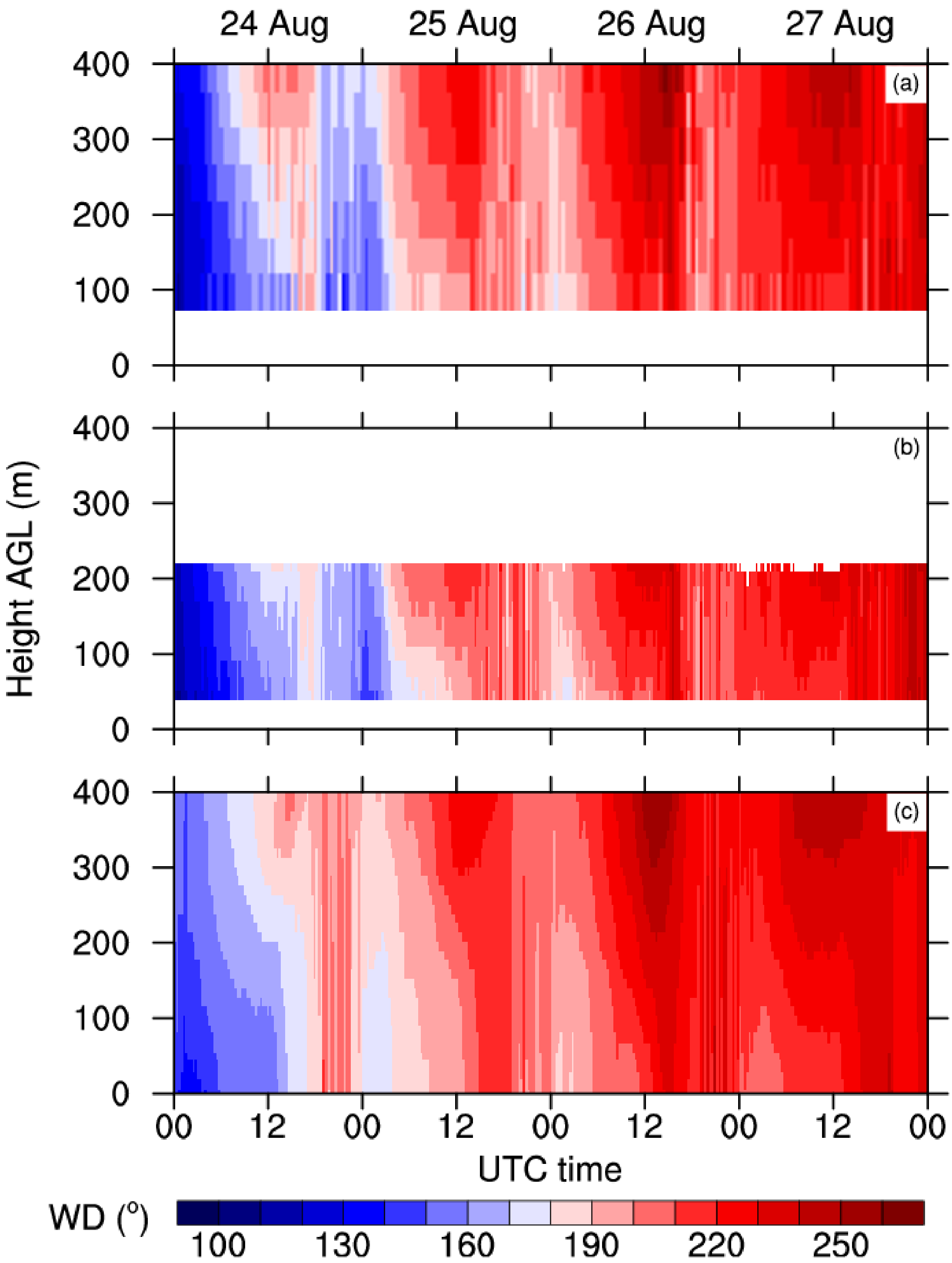
24 Aug
25 Aug
26 Aug
27 Aug
(a)
(b)
(c)
Height AGL (m)
0
100
200
300
400
00
12
00
12
00
12
00
12
00
UTC time
WD (°)
100
130
160
190
220
250

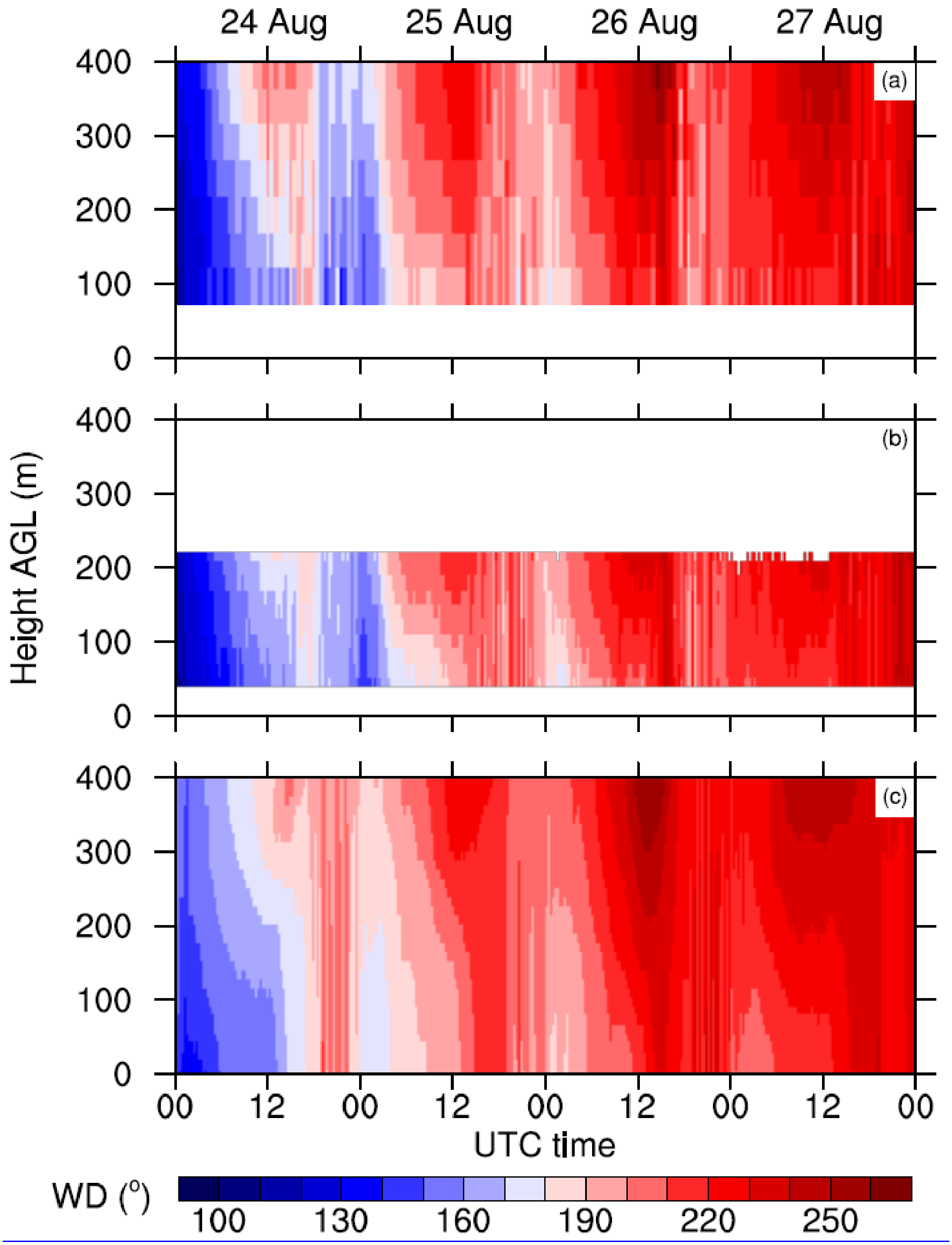

Figure 4: As in Fig. 3, but for WD.

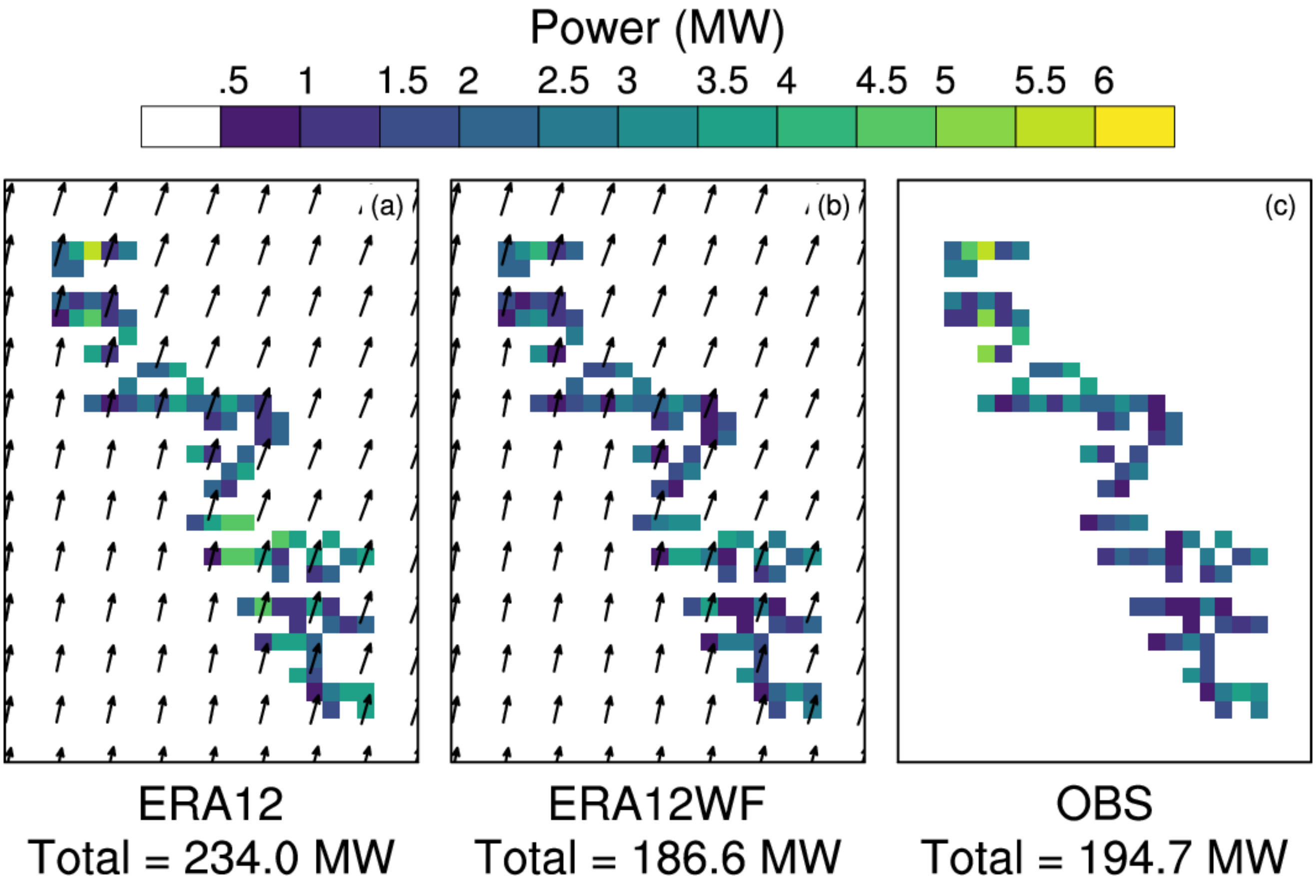
Power (MW)
.5
1
1.5
2
2.5
3
3.5
4
4.5
5
5.5
6
(a)
(b)
(c)
ERA12
Total = 234.0 MW
ERA12WF
Total = 186.6 MW
OBS
Total = 194.7 MW

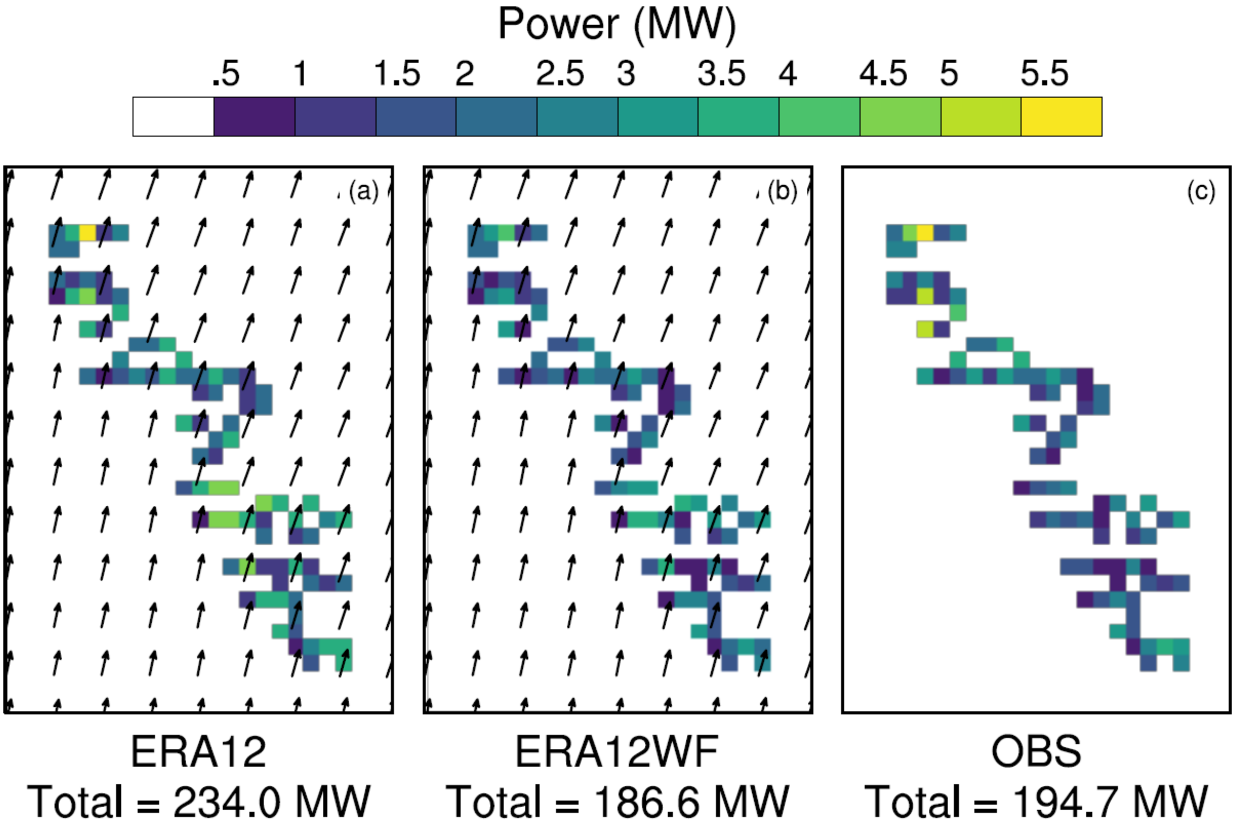

1085 **Figure 5: The power production for one 10-min period from the ERA12 estimates (a), the ERA12WF outputs (b) and the observation (abbreviated as OBS) (c). The total power in each grid cell is presented regardless of the number of turbines in each cell, and the wind-farm totals are summarized at the bottom. The vectors indicate the simulated winds, and their lengths correspond to the horizontal velocity magnitude.**

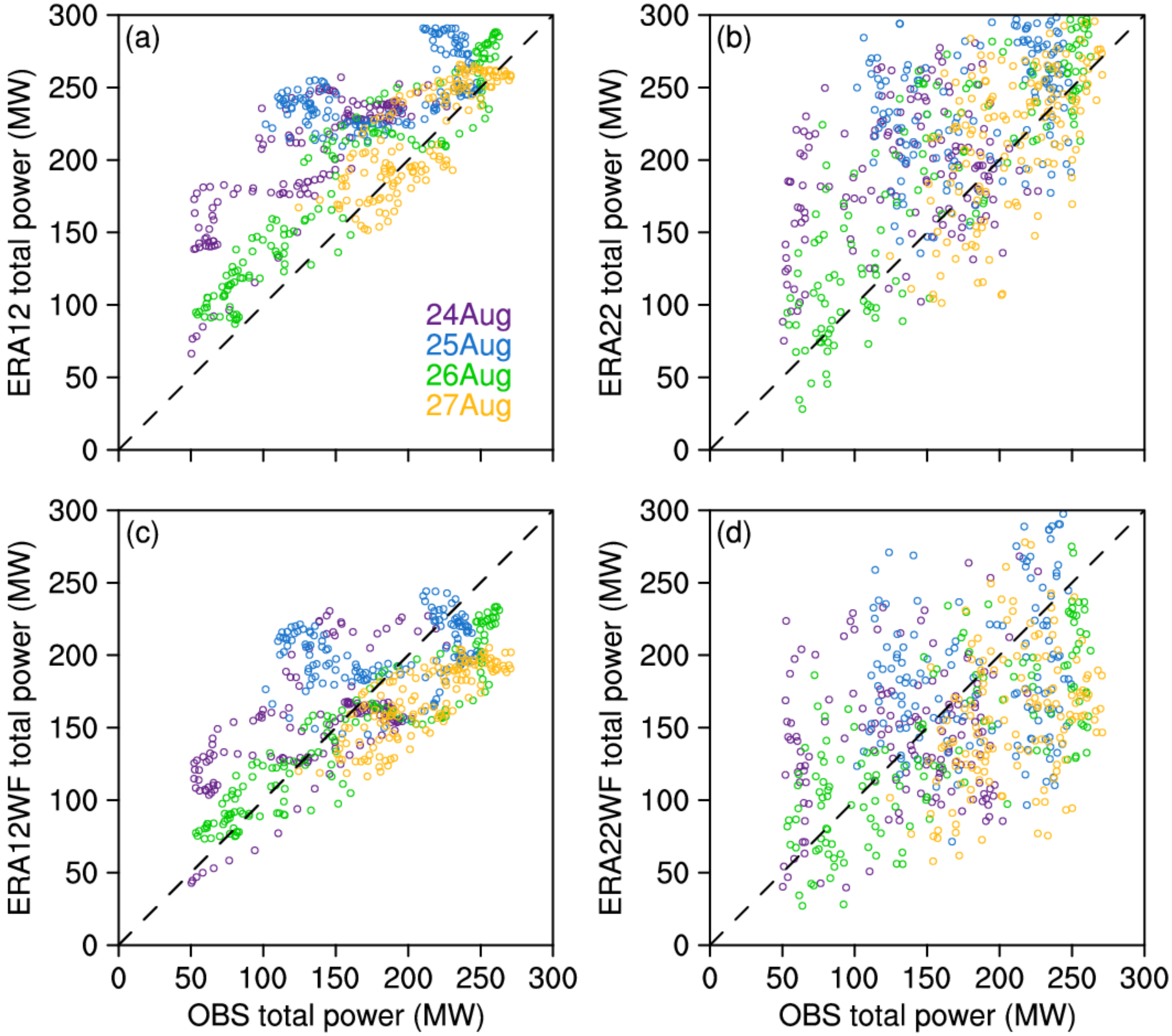

1090

Figure 6: Scatter plots comparing the 10-min average observed total power against the calculated total power from the ERA12 (a) and the ERA22 (b), and the simulated total power from the ERA12WF (c) and the ERA22WF (d). The dots represent the total power on 24 August (purple), 25 August (blue), 26 August (green) and 27 August (yellow).

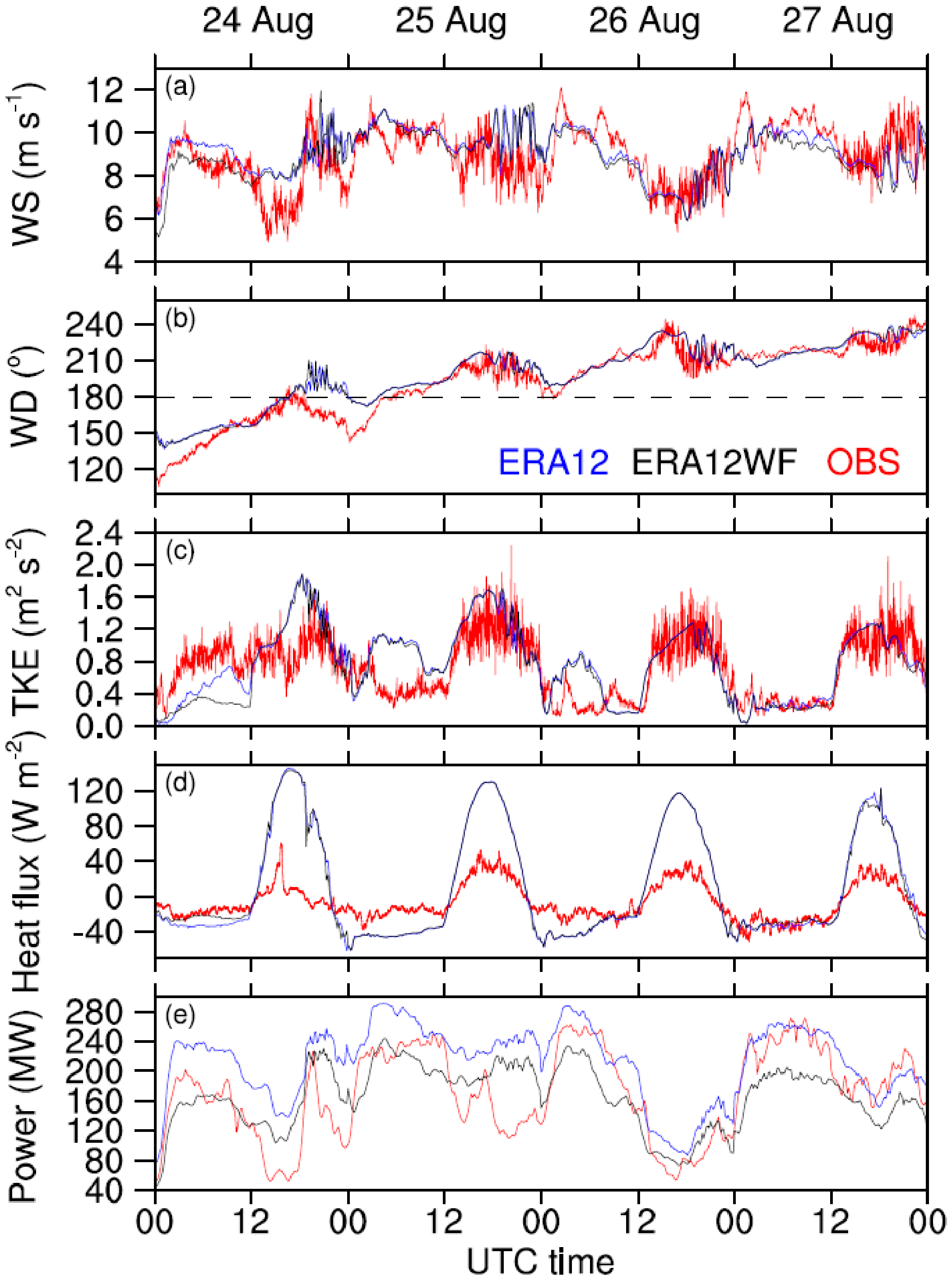
24 Aug
25 Aug
26 Aug
27 Aug
(a)
WS (m s^{-1})
4
6
8
10
12
(b)
WD (°)
120
150
180
210
240
ERA12
ERA12WF
OBS
(c)
TKE (m^2 s^{-2})
0.0
0.4
0.8
1.2
1.6
2.0
2.4
(d)
Heat flux (W m^{-2})
-40
0
40
80
120
(e)
Power (MW)
40
80
120
160
200
240
280
00
12
00
12
00
12
00
12
00
UTC time

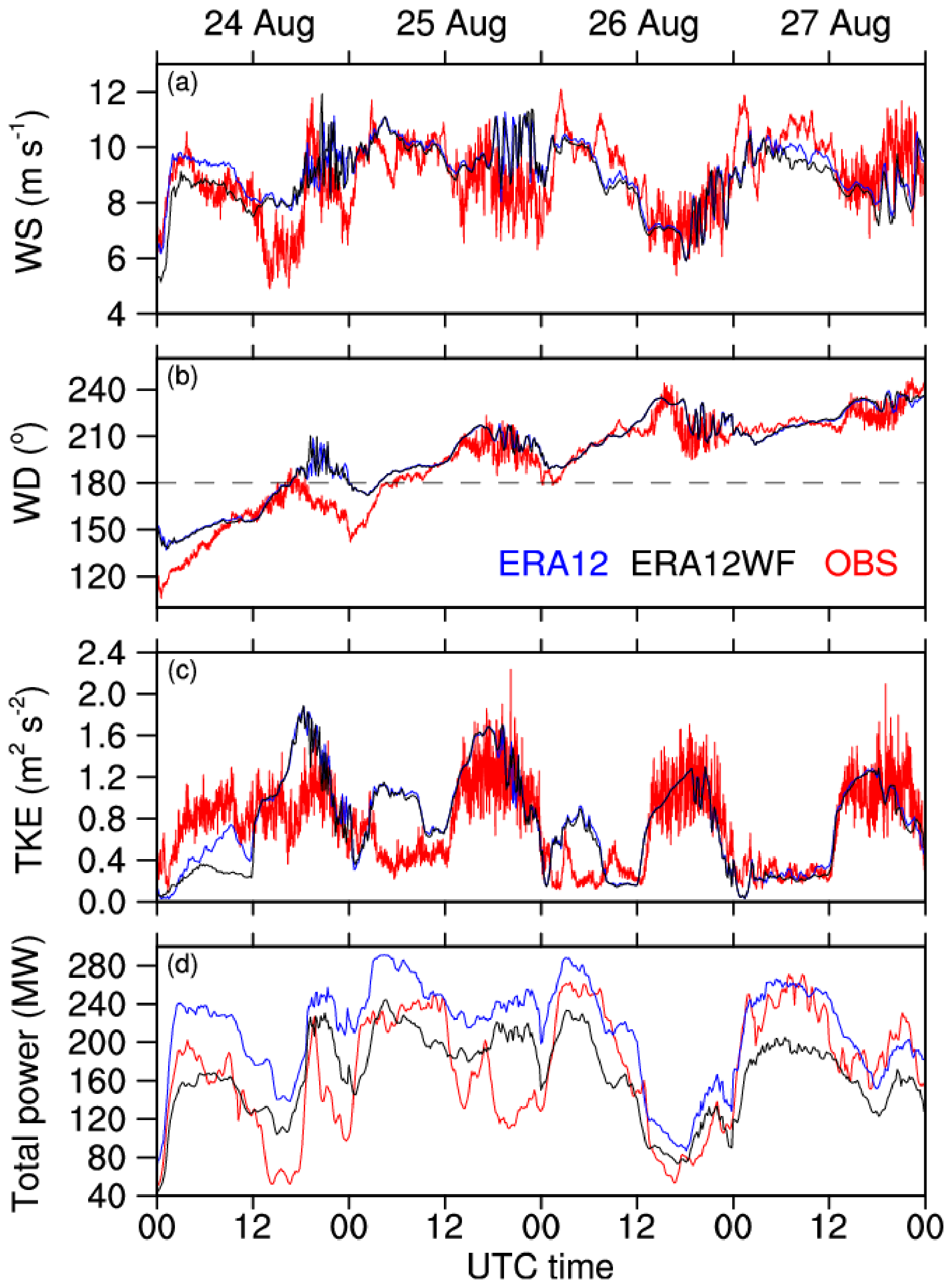

Figure 7: Time series of hub-height WS (a), hub-height WD (b), hub-height TKE (c), surface sensible heat flux (d), and total wind farm power (e~~d~~) from the ~~WC~~ measurements (in red) and the simulations (ERA12WF, in black; ERA12, in blue). The simulated values are interpolated to hub height at the grid point closest to the WC location. In (b), the grey horizontal dash line marks the WD of 180°. In (d), the grey horizontal dash line marks the heat flux of 0 W m^{-2}.

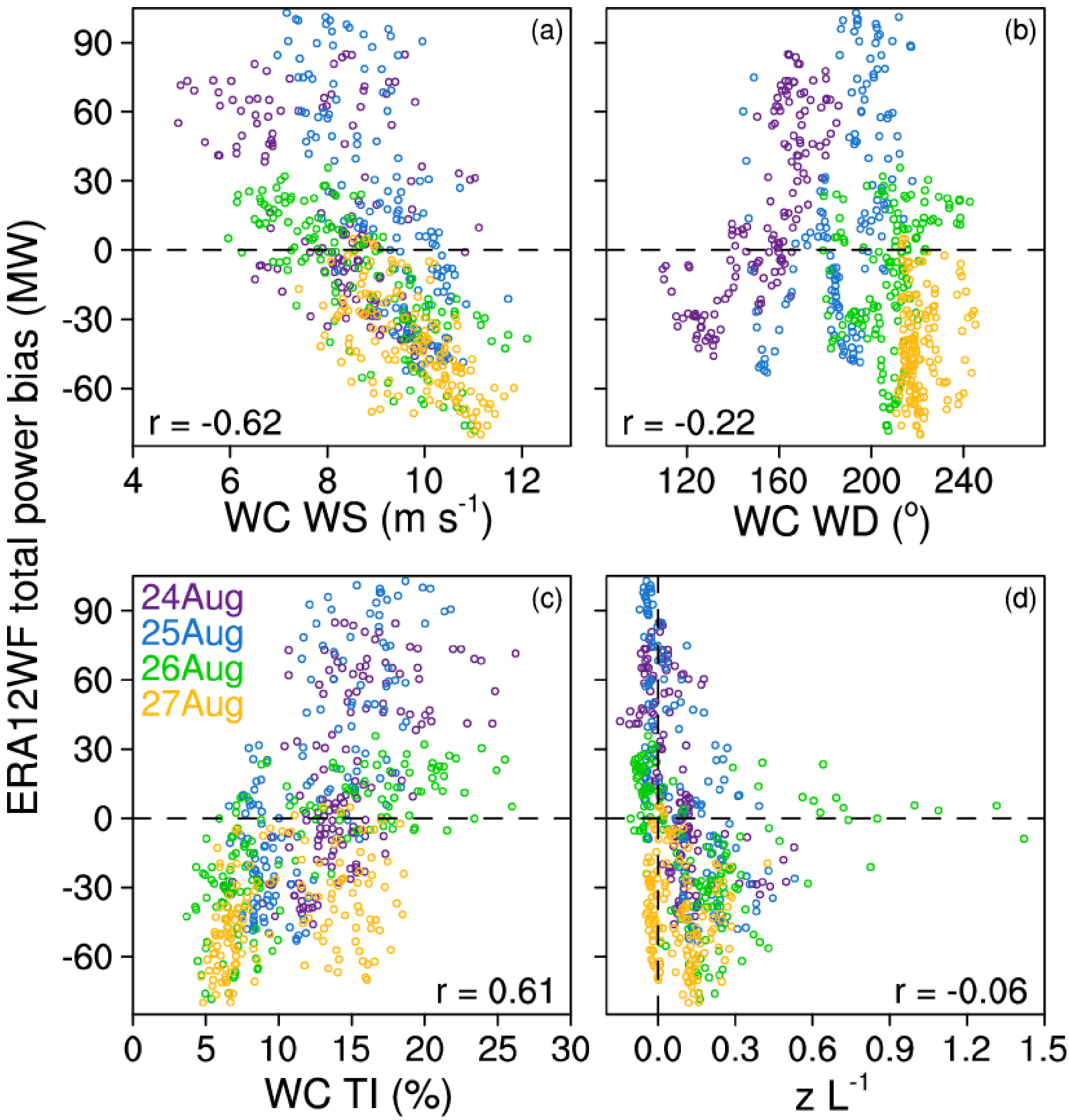

Figure 8: Scatter plots comparing the bias of the ERA12WF 10-min total power to the WC-observed hub-height WS (a), hub-height WD (b), hub-height TI (c) and stability parameter z L^{-1} measured at the surface flux station (d). The r represents the Pearson correlation coefficient. Similar to Fig. 6, different coloured dots represent biases on different days. The horizontal black dash lines mark the zero power bias, and the vertical black dash line in (d) at zero z L^{-1} differentiates the two stability regimes.

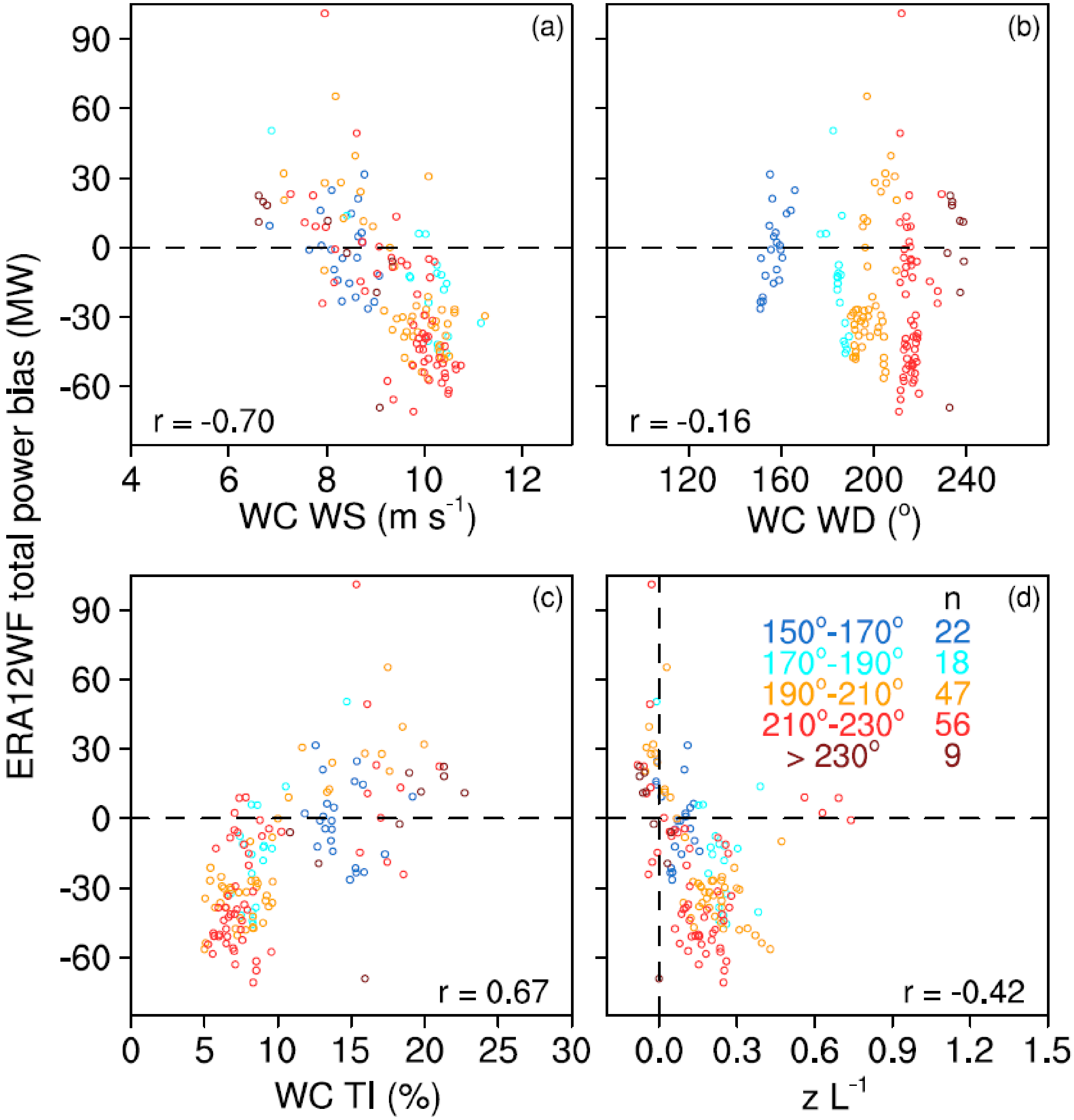

Figure 9: As in Fig. 8, and only including data when the winds are accurately simulated in the ERA12WF run: the modelled-observed absolute error in WS smaller than 1 $m s^{-1}$ and the absolute error in WD smaller than 5°. Different colours represent different WD bins: 150° to 170° in blue, 170° to 190° in cyan, 190° to 210° in orange, 210° to 230° in red, and 230° and beyond in maroon. The n values illustrate the respective sample size in each wind-direction bin.

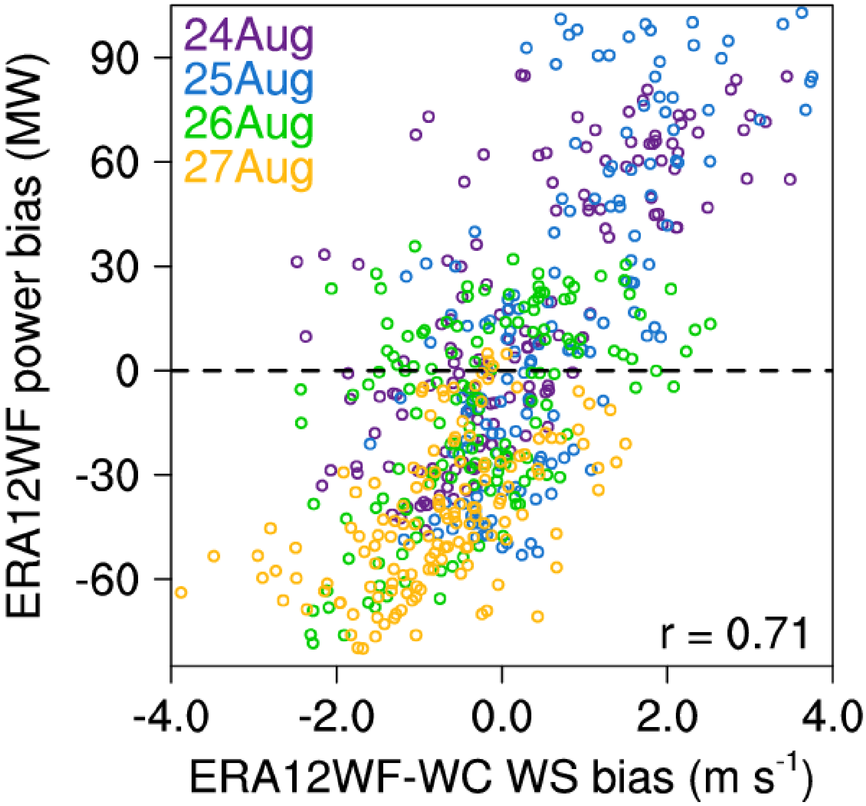

Figure 10: Scatter plot between the bias of the ERA12WF 10-min total power compared to observation, and its bias of the simulated hub-height WS in the closest grid cell to the WC. The r represents the Pearson correlation coefficient.

1115

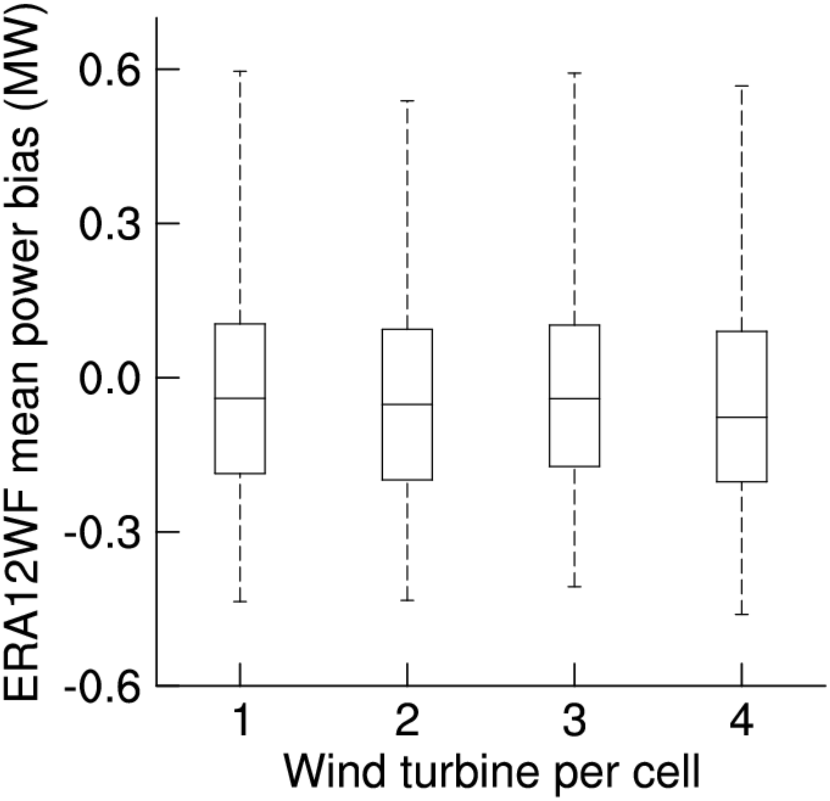

Figure 11: Boxplot of the average bias of the ERA12WF simulated power across different numbers of wind turbine per WRF grid cell every 10 minutes during the 4-day period.

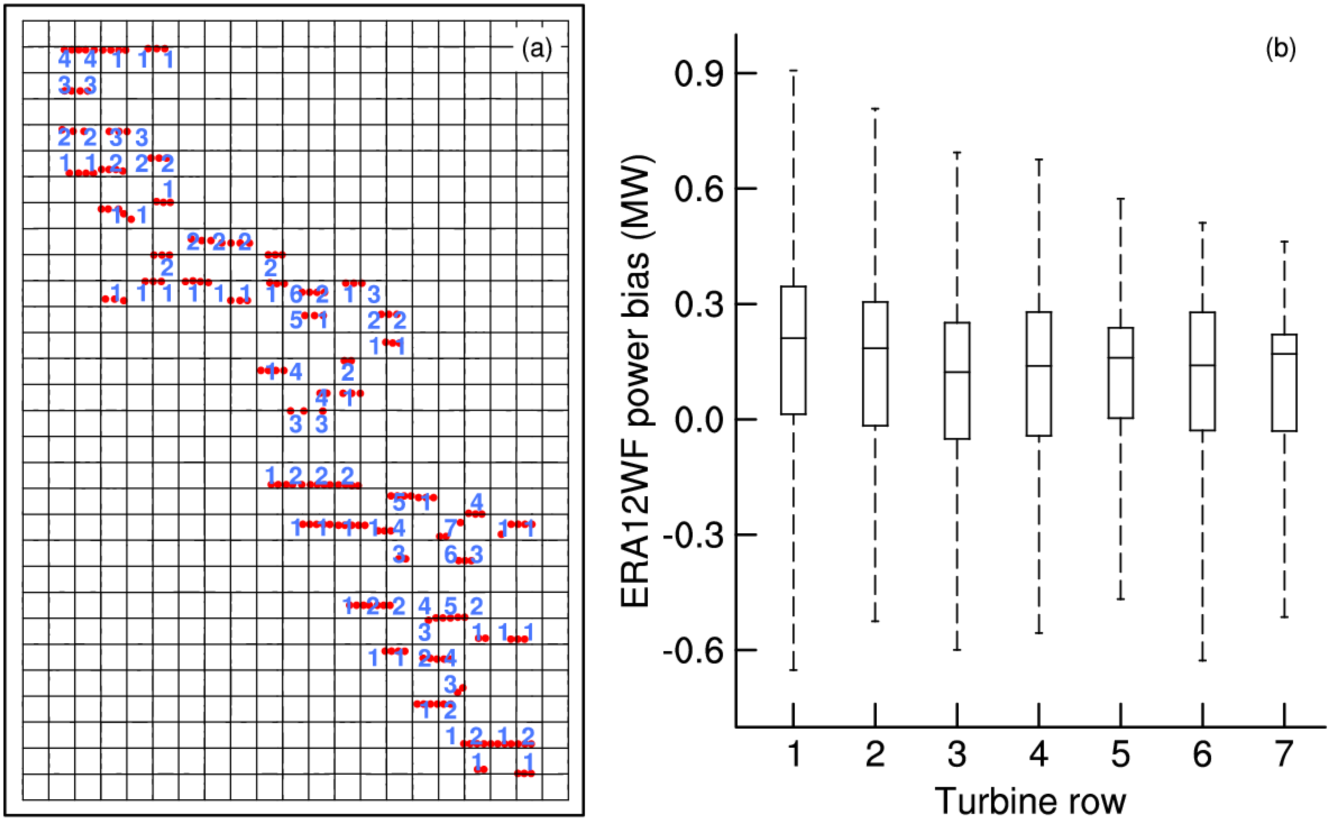

Figure 12: Map of the wind farm where the blue numbers represent the row number from the upwind row during southerly winds (a). The upwind row number is reset to 1 when the next two downwind grid boxes to the North contain no turbines. Boxplot of the average ERA12WF power bias normalized over different number of wind turbine rows, when the hub-height WD in the grid cell closest to the WC is between 175° and~~to~~ 185° (b).

Table 1: The WRF model configuration.

Parameterization	Scheme	Reference
Cumulus	Kain-Fritsch	Kain (2004)
Land surface	NOAH LSM	Ek et al. (2003)
Land surface roughness	Thermal roughness length	Chen and Zhang (2009)
Microphysics	Thompson aerosol-aware	Thompson and Eidhammer (2014)
PBL	MYNN Level 2.5	Nakanishi and Niino (2006)
Radiation	RRTMG	Iacono et al. (2008)

Table 2: List of WRF simulations and their features.

Run name	Boundary condition	Vertical resolution	WFP
ERA12	ERA-interim	12 m	No
ERA22	ERA-interim	22 m	No
GFS12	0.5° GFS	12 m	No
GFS22	0.5° GFS	22 m	No
ERA12WF	ERA-interim	12 m	Yes
ERA22WF	ERA-interim	22 m	Yes
GFS12WF	0.5° GFS	12 m	Yes
GFS22WF	0.5° GFS	22 m	Yes

Table 3: Average absolute error in WS (m s^{-1}) and WD (°) of different no-WFP runs.

	ERA12	ERA22	GFS12	GFS22
200S 120 m WS	1.49	1.84	**1.35**	1.54
WC 120 m WS	**1.21**	1.63	1.34	1.48
WC 80 m WS	**1.24**	1.64	1.36	1.55
WC 40 m WS	**1.47**	1.9	1.53	1.86
200S 120 m WD	14.99	15.98	**14.68**	14.99
WC 120 m WD	**12.66**	13.86	13.07	13.47
WC 80 m WD	**13.23**	14.55	13.85	14.24
WC 40 m WD	**14.19**	15.58	14.83	15.15

The smallest errors across different WRF settings are highlighted in bold.

Table 4: RMSE of 10-min total power (MW) of different model runs each day.

	24 Aug	25 Aug	26 Aug	27 Aug	4-day mean
ERA12	73.6	73.5	**35.4**	**22.6**	**51.3**
ERA22	79.5	**72.8**	48.5	41	60.5
GFS12	**62**	76.5	58.3	40.9	59.4
GFS22	73.9	89.6	65.3	51.9	70.2
ERA12WF	42.2	**49.4**	**31.1**	46.5	**42.3**
ERA22WF	61.7	61.2	50.9	71.6	61.4
GFS12WF	46.2	54.6	34.1	**36.1**	42.8
GFS22WF	**40**	60	32.6	37.3	42.5

Table 5: Average bias of 10-min total power (MW) of different model runs each day.

	24 Aug	25 Aug	26 Aug	27 Aug	4-day mean
ERA12	68.3	62.6	**26.8**	8.1	41.5
ERA22	58.3	**52.1**	28	**6.2**	**36.2**
GFS12	**49.4**	65	51.8	29	48.8
GFS22	65.5	80.7	60.3	35.8	60.6
ERA12WF	17.5	16.6	-12.2	-41.6	-4.9
ERA22WF	10.4	**0.6**	-17.6	-53.6	-15.1
GFS12WF	3.8	22.2	**9.6**	-18.6	**4.3**
GFS22WF	**2.9**	29.7	10.9	**-12.3**	7.8

The RMSEs and biases closest to zero across different days are highlighted in bold.

Table 6: Differences (first value) and p-values (second value) from 2-sample t-tests of simulated power from different ERA runs.

		ERA12	ERA12WF	ERA22WF
	4-day mean	41.8	-4.9	-15.1
ERA12	41.9		-46.8; 0	
ERA22	36.1	5.7; 0.0300		-51.2; 0
ERA12WF	-4.9			
ERA22WF	-15.1		10.2; 9.60×10^{-4}	

Table 7: As in Table 6, but for GFS runs.

		GFS12	GFS12WF	GFS22WF
	4-day mean	48.6	4.2	7.8
GFS12	48.6		-44.4; 0	
GFS22	60.6	-12.0; 1.09×10^{-7}		-52.8; 0
GFS12WF	4.2			
GFS22WF	7.8		-3.6; 0.163	

Table 8: P-values from 2-sample t-tests of the 10-min observed power and the 10-min simulated power from different model runs.

	Simulated 4-day mean	Observed 4-day mean	Difference of means	P-value
ERA12	212.7	170.9	41.8	0
ERA22	207.0		36.1	0
GFS12	219.5		48.6	0
GFS22	231.4		60.5	0
ERA12WF	166.0		-4.9	0.106
ERA22WF	155.8		-15.1	6.54×10^{-6}
GFS12WF	175.1		4.2	0.167
GFS22WF	178.7		7.8	0.0136